Mesoscale functional architecture in medial posterior parietal cortex

Riichiro Hira[1,3,4,*], Leah B. Townsend[3], Ikuko T. Smith[2], Che-Hang Yu [1], Jeffrey N. Stirman[3], Yiyi Yu[1], and Spencer LaVere Smith[1,3,*]

1. Department of Electrical and Computer Engineering, University of California Santa Barbara.
2. Department of Molecular, Cellular, and Developmental Biology, Department of Psychology and Brain Sciences, University of California Santa Barbara.
3. Neuroscience Center, University of North Carolina Chapel Hill.
4. Department of Physiology and Cell Biology, Tokyo Medical and Dental University.
* Correspondence and requests for materials can be addressed to S.L.S. (email: sls@ucsb.edu) or R.H. (email: rhira.phy2@tmd.ac.jp)

Abstract

The posterior parietal cortex (**PPC**) in mice has various functions including multisensory integration, vision-guided behaviors, working memory, and posture control. However, an integrated understanding of these functions and their cortical localizations in and around the PPC and higher visual areas (**HVAs**), has not been completely elucidated. Here we simultaneously imaged the activity of thousands of neurons within a 3 x 3 mm^2 field-of-view, including eight cortical areas around the PPC, during behavior. Mice performed both a vision-guided task and a choice history-dependent task, and the imaging results revealed distinct, localized, behavior-related functions of two medial PPC areas. Neurons in the anteromedial (**AM**) HVA responded to both vision and choice information, and thus AM is a locus of association between these channels. By contrast, the anterior (**A**) HVA stores choice history with rotational dynamics and represents posture. Mesoscale correlation analysis on the intertrial variability of neuronal activity demonstrated that neurons in area A shared fluctuations with S1t (trunk primary somatosensory area), while neurons in AM exhibited diverse, area-dependent interactions. Pairwise interarea interactions among neurons were precisely predicted by the anatomical input correlations, with the exception of some global interactions. Thus, the medial PPC has two distinct modules, areas A and AM, which each have distinctive modes of cortical communication. These medial PPC modules can serve separate higher-order functions: area A for transmission of information including posture, movement, and working memory; and area AM for multisensory and cognitive integration with locally processed signals.

Introduction

The posterior parietal cortex (PPC) is an association area located between the visual and somatosensory cortices and is widely shared by mammals. The PPC has distinct regions and each one of the regions has unique functions and corticocortical projection patterns in primates (Cavada and Goldman‐Rakic 1989, Rizzolatti, Fogassi et al. 1997, Freedman and Ibos 2018). In mice, the PPC can overlap with HVAs (Wang and Burkhalter 2007), has characteristic cytoarchitectures (Franklin and Paxinos 2001, Hovde, Gianatti et al. 2018, Lyamzin and Benucci 2019, Gilissen, Farrow et al. 2021), unique corticocortical recurrent projection patterns (Harvey, Coen et al. 2012, Odoemene, Nguyen et al. 2017, Hovde, Gianatti et al. 2018), which are similar to that of rats (Whitlock, Sutherland et al. 2008, Olsen and Witter 2016). Despite its relatively small areas compared to that of primates, mouse PPC has various functions like primates including navigation (Harvey, Coen et al. 2012, Morcos and Harvey 2016, Driscoll, Pettit et al. 2017, Runyan, Piasini et al. 2017, Krumin, Lee et al. 2018, Minderer, Brown et al. 2019, Tseng, Chettih et al. 2022), multisensory integration (Olcese, Iurilli et al. 2013, Yoshitake, Tsukano et al. 2013, Song, Kim et al. 2017), memory-guided decision making (Harvey, Coen et al. 2012, Funamizu, Kuhn et al. 2016, Goard, Pho et al. 2016, Driscoll, Pettit et al. 2017, Pho, Goard et al. 2018), visually (Odoemene, Pisupati et al. 2018) and auditory (Funamizu, Kuhn et al. 2016, Zhong, Zhang et al. 2018) guided decision making. In rats, PPC is also important in attention (Reep and Corwin 2009, Yang, Jacobson et al. 2017), sensory history (Akrami, Kopec et al. 2018), and posture coordination (Mimica, Dunn et al. 2018). Thus, neurons in rodent PPC can represent various sensorimotor and integrative functions. However, prior studies typically focused on a single cortical location and often a single function, and thus it is unclear whether neurons with particular functions are distributed in overlapping populations or localized.

The function of an individual cortical area is influenced by what information that area receives from other brain regions. Connectivity among cortical areas is highly specific in mice (Oh, Harris et al. 2014), and includes frequent cases of neurons sending bifurcated axons to multiple target regions (Han, Kebschull et al. 2018). This axonal divergence indicates that to understand association inter-area interactions, it is insufficient to consider only pairwise connections. Instead, such analysis should consider the shared connectivity patterns among three or more areas. When weak connections are included, the mouse cerebrum is estimated to have a 97% connectivity density (Gămănuţ, Kennedy et al. 2018). In addition, cortical activity is a complex interplay of diverse information due to interactions with the thalamus, basal ganglia, and cerebellum. Moreover, the mode of these interactions can vary depending on behavior (Bressler and Kelso 2001, Avena-Koenigsberger, Misic et al. 2017). Thus, to understand the nature of the PPC, it is necessary to examine not only the pairwise interaction between cortical areas, but also investigate multiple interrelated areas in an integrated manner under a variety of environmental constraints.

Here, we examine the functional architecture of the mouse PPC and surrounding cortical areas using calcium imaging with a large field-of-view two-photon microscope (Yu, Stirman et al. 2021) during head-fixed behavior in multiple tasks. We mapped vision, choice, choice history, and posture-related neurons within and surrounding the PPC. We found clear functional localization between two areas in medial PPC: HVAs A and AM. Furthermore, the mesoscale correlation structure of trial-to-trial variability indicated that A and AM had distinct relationships with surrounding cortical areas. The local interarea interaction aligned with the anatomical structure, but the global interaction did not, and thus the functional data revealed an aspect of the circuit organization. Our findings indicate that various modes of interarea communication constitute diverse functions of PPC.

Results

1. Demarcation of PPC as A, AM, and RL

To functionally determine the precise anatomical location of PPC, we first identified retinotopic and somatotopic organizations with intrinsic signal optical imaging (ISOI) in anesthetized mice (Kalatsky and Stryker 2003, Smith and Trachtenberg 2007, Marshel, Garrett et al. 2011, Smith, Townsend et al. 2017, Yu, Stirman et al. 2018). Retinotopic mapping revealed locations of each HVA including AM (**Fig. 1a**), which has

been considered to be the core of mice PPC in recent studies (Krumin, Lee et al. 2018, Odoemene, Pisupati et al. 2018). To map the portion of the primary somatosensory (**S1**) area anterior to the HVAs, we used tactile vibration of the tail and trunk in the same animal. The trunk region of S1 (**S1t**) is located at a posterior region within S1 in mice (**Fig. 1b**). The distance from the center of the AM to the center of the S1t was ~900 μm (894 ± 18.3 (mean ± s.d.), n = 8 mice). Assuming that the diameter of AM and S1t are 600 μm and 400 μm, respectively, we could estimate that there would be a space 400 μm wide along the rostrocaudal axis between these two areas. Here, we defined this space as area A (**Fig. 1c**), because it roughly overlaps with the HVA identified as area A in a landmark anatomical study of mouse HVAs (Wang and Burkhalter 2007). Our definition of area A likely includes a larger area than this original definition.

Often, PPC is determined using stereotaxic coordinates, and we considered this approach. However, systematic mapping of visual areas relative to the lambda and midline showed that each HVA location based on the stereotaxic coordinates was unreliable. The mean distance from the center position of each HVA in each mouse to the average center position across mice was 244 μm, (range: 198 – 316 μm, n = 12 mice) (**Supplementary Figure 1a,b**) when the positions were measured relative to the lambda landmark. We confirmed that the variability in locations was not explained by the age or sex **(Supplementary Figure 1c**). Instead, the variation of HVAs substantially decreased after the registration of the areas by translation based on the location of V1 and RL. After this registration, the mean distance from the center position of each HVA to the average center position across mice was ~91.5 μm (range: 38.6 - 141 μm), n = 12 mice): a reduction in variability by more than half **(Supplementary Figure 1d-f)**. This improvement indicates that relative locations of HVAs are similar across mice (Waters, Lee et al. 2019), but HVA locations relative to skull landmarks are more than twice as variable. Thus, localizing these small HVAs and components of PPC by stereotaxic coordinates can introduce variability and decrease the fidelity of localization. We concluded that functional imaging of retinotopic and somatotopic organization must be obtained in each individual mouse to precisely and rigorously map HVAs and PPC, and to ascribe functions to neurons therein.

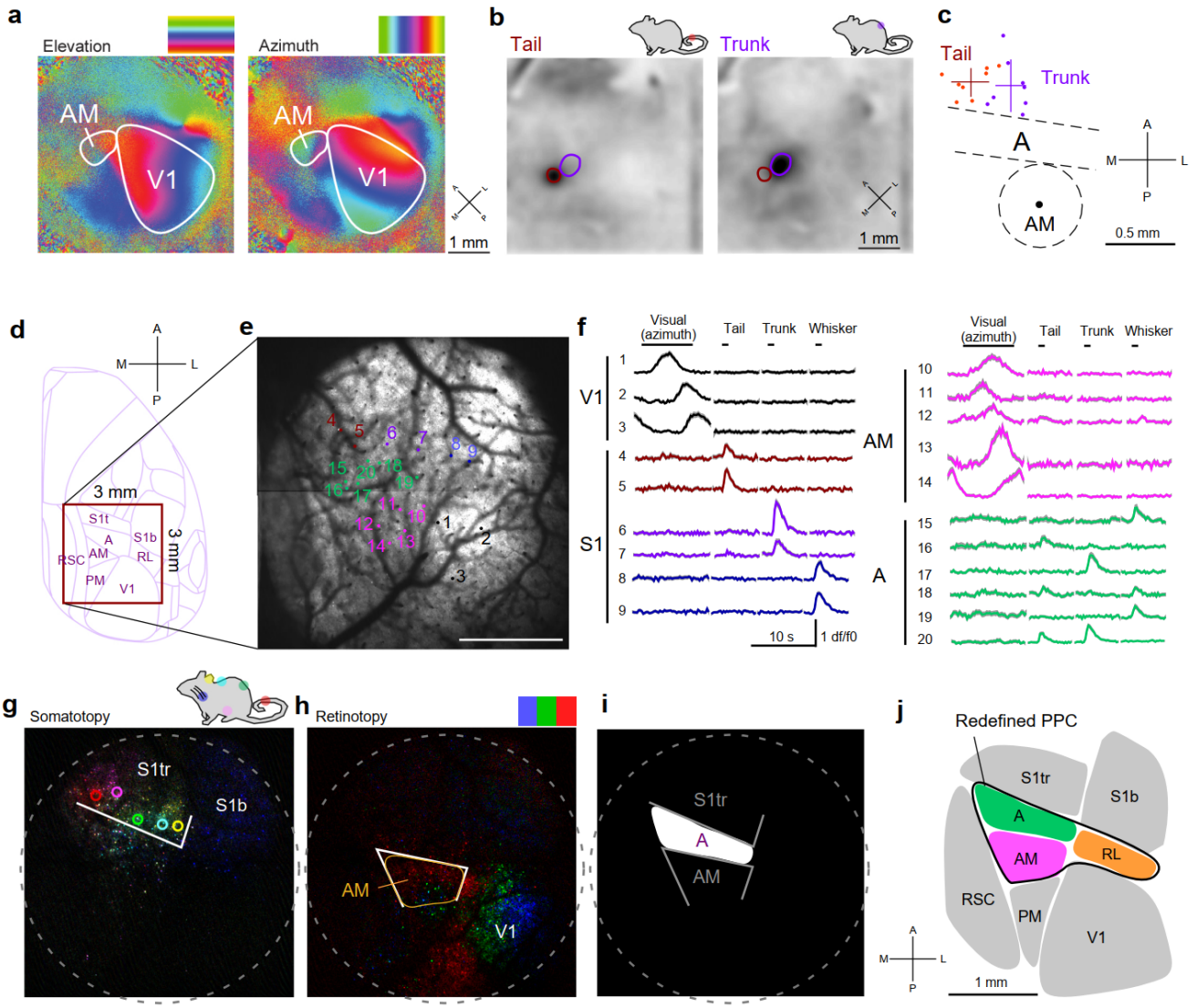

Figure 1. Definition of cortical area A and redefinition of PPC based on visual and somatosensory responses. a. Elevation *(left)* and azimuth (*right*) maps showing retinotopy that form the borders of V1 (primary visual cortex) and AM. The cortical surface was color-coded according to the location of the bar on the monitor at the time of the evoked visual response. **b.** Tactile stimuli of a tail (left, red) and a trunk (*right*, green) resulted in clear spots in S1. **c.** The center positions of S1 tail and S1 trunk regions relative to the center position of AM from 8 mice. The gap space between the S1 trunk region and AM was defined as A. **d.** A location of the cranial window and FOV of two-photon imaging was overlaid on the Allen CCF version 3 (Oh, Harris et al. 2014). **e.** The average image of calcium imaging and ROI positions for panel **f**. **f**. Fluorescence traces (mean and s.e.m.) of ROI indicated in panel **e** when the mouse received visual stimulation (azimuth) and tactile stimuli (tail, trunk, and whisker). **g,h**. Single neuron resolution mapping of somatotopy (**g**) and retinotopy (**h**) revealed that A had neither retinotopy nor somatotopy, but had neurons activated by tactile stimuli and a small number of neurons activated by the visual stimulation. On the other hand, AM had a retinotopy and a small number of neurons activated by tactile stimuli. **i.** A was defined after the S1 and AM was determined by somatotopic and retinotopic organizations, respectively. **j**. Redefined PPC in this study (A, AM and RL).

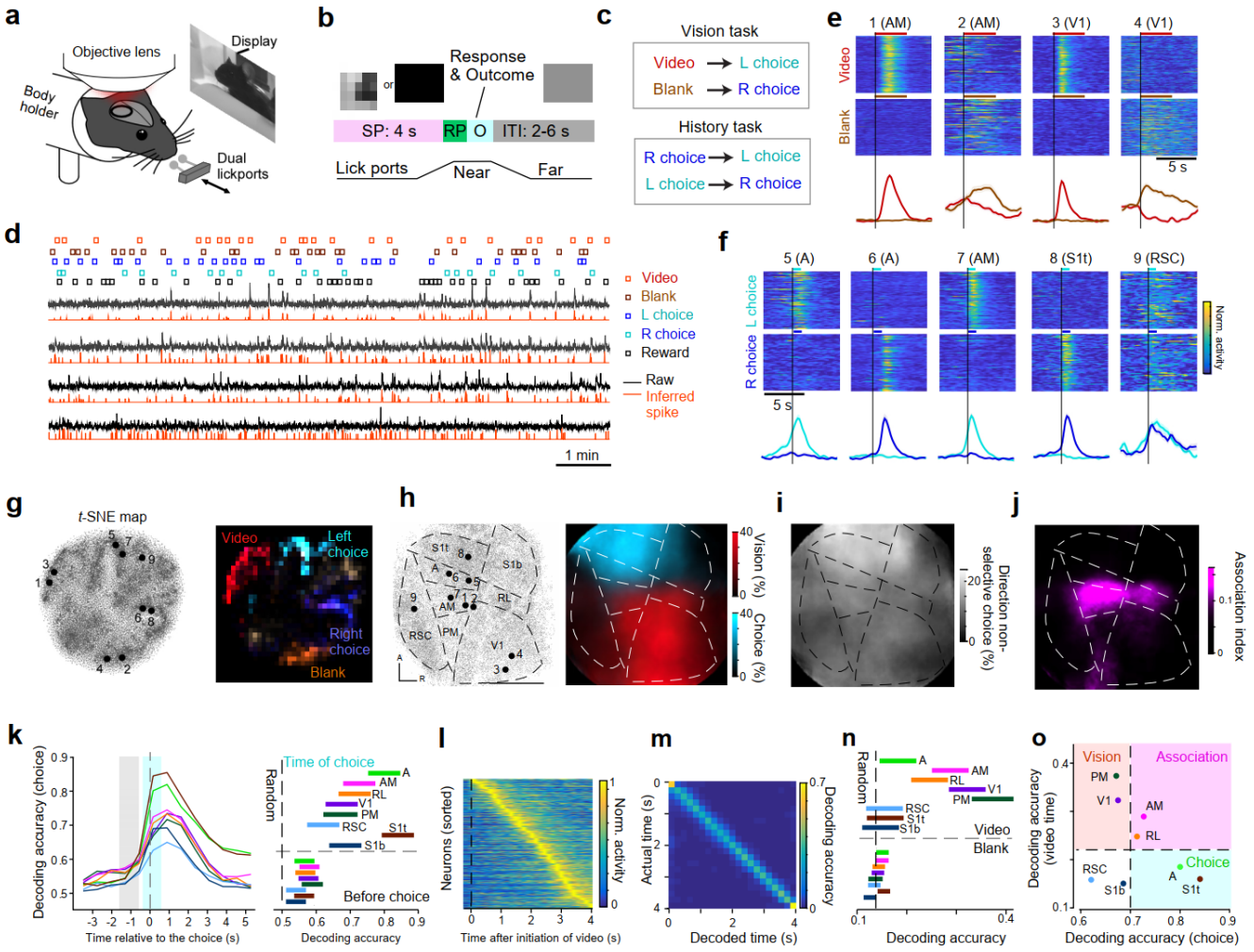

Figure 2. Vision and choice information are merged in AM. a. Schematic illustration of a vision-guided choice task. **b.** The lick-ports approached after a 4-s sampling period (SP). The mouse was given a reward (water) or a punishment (air-puff) based on the licking direction during response period (RP). ITI, Inter-trial-interval. **c.** Rules of vision and history task. **d.** Four example raw traces (black) and inferred spikes (red) during the task. **e.** Representative vision neurons (ROI 1-4 in **h**). **f.** Representative choice neuron (ROI 5-8 in **h**) and a non-selective neurons (ROI 9). **g.** *t*-SNE result of single neuron activities (left). Task-related neurons were mapped onto the *t*-SNE (right). **h.** All recorded location of neurons (left) and the ratio of vision and choice neurons (right). **i.** Percentage of non-selective neurons activated during choice. **j.** Map of Association index (harmonic mean of vision and choice neurons.) **k.** Decoding accuracy of choice by activity of 50 neurons from eight areas before and after the choice were plotted (left). The decoding accuracies 1s before (right bottom, gray shade; p=0.13; one-way ANOVA) and just after (right top, blue shade; $p=3.6 \times 10^{-9}$; one-way ANOVA) the choice was shown. **l.** The activity of vision neurons was averaged and aligned by the order. **m.** The time after onset of the video was precisely decoded with population of vision neurons in panel **l**. **n.** Decoding accuracy of time during video presentation (top; $p=1.1 \times 10^{-15}$; one-way ANOVA) and black screen presentation (bottom; p=0.013; one-way ANOVA) were plotted. **o.** Decoding accuracies of time in video presentation and choice direction indicate that AM would be the best position for associating these two signals. Error bars, mean ± s.e.m. in **e** and **f**, 95% confidence interval in **l** and **n**.

ISOI was supplemented with two-photon calcium imaging to observe the activity of neurons within and surrounding PPC including area A (**Fig. 1d-f**). In awake mice, somatosensory stimuli including tail, trunk, neck, and whiskers resulted in responses in PPC areas. In S1, somatosensory stimulation evoked localized neuronal responses that exhibited somatotopic organization. In contrast, area A neurons activated by somatosensory stimuli did not exhibit clear somatotopy (**Fig. 1g**). Likewise, visual responses of neurons in area A did not exhibit clear retinotopy (**Fig. 1h**), in contrast to other HVAs (Wang and Burkhalter 2007). Some

area A neurons showed activity by stimulation of multiple body parts such as trunk and tail, or trunk and whiskers (**Fig. 1f**). Thus, area A can integrate multiple somatosensory inputs, potentially contributing to body coordination (e.g., posture) (Mimica, Dunn et al. 2018). Some neurons in AM were activated by tactile stimuli, and again this activity lacked somatotopy. Based on the multisensory responsiveness of areas A, AM, and RL (Olcese, Iurilli et al. 2013, Itokazu, Hasegawa et al. 2018, Mohan, de Haan et al. 2019), we demarcate the PPC as a three module structure, consisting of AM, RL, and A (as defined above) (**Fig. 1j**).

2. Visually guided task

After precisely mapping PPC and adjacent cortical areas, we examined layer 2/3 neuronal activity during behavior with single neuron precision across multiple cortical areas simultaneously with large field-of-view, two-photon calcium imaging. We used transgenic mice that express a genetically encoded calcium sensor, GCaMP6s, in cortical neurons (Chen, Wardill et al. 2013). The field-of-view (**Supplementary Figure 2**) typically covered PPC and surrounding areas including HVAs, V1, S1, and a portion of retrosplenial cortex (RSC).

PPC has been reported to have functions including visually guided decision-making and working memory. Do these functions differ among RL, A, and AM? To address this question, we trained the mice in head-fixed conditions to perform vision-guided and history-guided two-alternative forced-choice tasks (**Supplementary Figure 3a-e**) and imaged the activity of neurons for each task. First, we investigated the distribution of task-related neurons during a visually-guided task ("**vision task**"; **Fig. 2a-c**). In this task, mice had to lick one of two waterspouts (left or right) based on the visual stimuli, naturalistic video or black screen, presented to the left visual field of the mice (imaging in the right hemisphere) (**Supplementary Figure 3f,g**). This simple task was designed to clearly map sparse responses of neurons to natural video (Froudarakis, Berens et al. 2014), and to map the choice-related activity guided by the visual stimuli at the same time to see segregation or overlapping of the vision and choice-related neurons around PPC.

Large field-of-view calcium imaging during the task enabled us to simultaneously observe ~10^4 neurons (n = 5 mice, total of 10 sessions, 47162 neurons). Neurons were robustly activated by specific frames in the naturalistic video, by the black screen, or by left or right choice (**Fig. 2d,e; Movie 1**). Notably, some PPC neurons showed complex dynamics rather than simply encoding specific visual or choice information, indicating integrative roles. To quantitatively identify and map the functional properties of each neuron, we constructed a linear regression model (**"encoding model"**, **Supplementary Figure 4a**). In the encoding model, the activity of each neuron was fitted by a weighted sum of the external control parameters such as a video frame and behavior parameters such as choice and reward directions. The statistical significance ($p<0.001$) of each parameter corresponding to visual stimulus and chosen direction was used to identify the vision and choice-related neurons, respectively. The functional labels revealed by this encoding model were consistent with the *t*-SNE clusters, indicating the validity of the encoding model (**Fig. 2f**). The neurons which were selective to video or black screen (**"vision neurons"**) were found in V1 and HVAs including AM, while the neurons which were selective to the chosen direction (**"choice neurons"**) were distributed in S1t and A (**Fig. 2g**). Interestingly, the neurons that activated during choice period irrespective of the choice directions were distributed broadly (**Fig. 2h**). The vision and choice neurons distributed mostly exclusively, but some overlapping was found around AM as revealed by mapping of the harmonic mean of the percentage of vision and choice neurons (**"association index"**) (**Fig.2i**). This indicates that the AM would be suitable for integrating vision and choice information rather than the A, RL or the other areas around PPC.

The PPC neurons had been thought to be important for decision making, but recently it is also suggested that the PPC neurons store the history information rather than deciding upcoming choice. To analyze whether the neurons around PPC represent the upcoming choice or the past choice in our visually guided task, we decoded the choice direction with activity of 50 neurons before and after the choice (**Fig. 2j**). The decoding accuracies of A and S1 were higher than the other areas at the choice timing and they stored the choice information even 5 s after the choice. On the other hand, the decoding accuracy of the choice 1 s before the

choice were very low in any areas recorded. Thus, neurons in areas A and S1t reflect the choice direction immediately after the choice and store it over 5 s. In addition, vision neurons preferred a specific time of the video frame resulting in the vision neurons sequentially firing during the sampling period (**Fig. 2k**). Decoding analysis showed that the vision neurons precisely possessed the temporal information of the video frame (**Fig. 2l**). Such precise decoding of time during sampling period was not observed in black screen trials (**Fig. 2m**). From the two decoding performances, we divided the imaged areas into four groups (**Fig. 2n**). Note that area AM is the most suitable area for the association of these two parameters, as it possesses a substantial amount of decodable information about both parameters.

3. Choice history guided task

Next, we asked whether and where choice history information can be stored in PPC and surrounding areas. We designed a choice history-dependent task ("**history task**") with the same set up as the vision task (**Fig. 2a-c**). In this task, the mice had to choose the opposite side of the previous choice. Mice had to store the direction of the choice for 6-10 seconds from the previous choice to the next choice including an inter-trial-interval (**ITI**) and a sampling period. Since the visual stimuli were randomly presented during the sampling period, the mice had to ignore the visual stimuli. This task was designed to map the history neurons in contrast to the choice neurons and the vision neurons around PPC.

Large FOV calcium imaging during the history task (n=4 mice, 10 sessions, 27059 neurons) revealed that neurons in A and S1t maintained their activity during the ITI in a past-choice-specific manner, indicating that these neurons stored the choice history for making the next choice (**Fig. 3a**). We used the same encoding model as used for the vision task to identify the neurons representing the history of the previous choice (**"history neurons"**) as well as choice and vision neurons. Again, the functional labels revealed by this encoding model were consistent with the t-SNE clusters, indicating the validity of the encoding model (**Fig. 3b**). We found that neurons in area A had significantly larger ratio of history neurons than all the other areas including S1t that have more choice neurons, and that neurons in AM exhibit large association index (**Fig. 3c,f**). We also found more history neurons in the history task in A compared to those in the vision task (**Fig. 3e**). Thus, A exhibited a task-specific functional change, preferentially representing a parameter when it is relevant, despite being available in both tasks.

PPC neurons are known to store the information of not only the choice history but the outcome and sensory histories (Morcos and Harvey 2016, Akrami, Kopec et al. 2018). We compared these candidates by decoding analysis (**Fig. 3f,g**). Although the outcome and visual information rapidly decreased in all areas after a trial, the choice information was strongly represented in A and S1t, and stored during the ITI, especially in A. We confirmed that the choice history information was on the past rather than on the future in both A and S1t (**Fig.3h**). We also asked whether the history neurons in A contributed to the working memory. When the next trials were correct, the decoding accuracy from history neurons in A during the ITI stayed higher than when the next trials were incorrect (**Fig. 3i**). Thus, the choice history information possessed by history neurons led the animal to the correct choice in following trials. In other words, the history neurons exhibited properties of working memory.

What kind of dynamics did the history neurons use to store this choice history information? The population activity of the history neurons indicated that each history neurons had a specific time of the peak activity, resulting in the sequential activity after the choice (**Fig. 3j**). In this task, left and right selection is alternated, so the activity of the history neuron will be a sequence that repeats in two consecutive trials. We used jPCA to visualize and quantify this activity pattern (**Fig. 3k**). As expected, the population of history neurons showed one-round rotational dynamics in two trials, and the same was true for the A population, but the AM population did not show rotational dynamics. The R^2 of M_{skew}, which indicates the extent to which population dynamics can be explained by rotational dynamics, in A and S1t was not only higher than that in the other areas (**Fig. 3l**) but also significantly correlated with the correct rate of the session (**Fig. 3m**). Interestingly, the sequential activity was also observed in AM, but it was less specific to the choice (**Fig. 3n**), resulting in the decoding accuracy of time after specific choice was much higher in A than in AM, while the decoding rate of the time

with incorrect choice was higher in AM than in A (**Fig. 3o**). These results indicate that the history-related activities of A and S1t encode past behavior histories by creating long sequences, and that these rotational

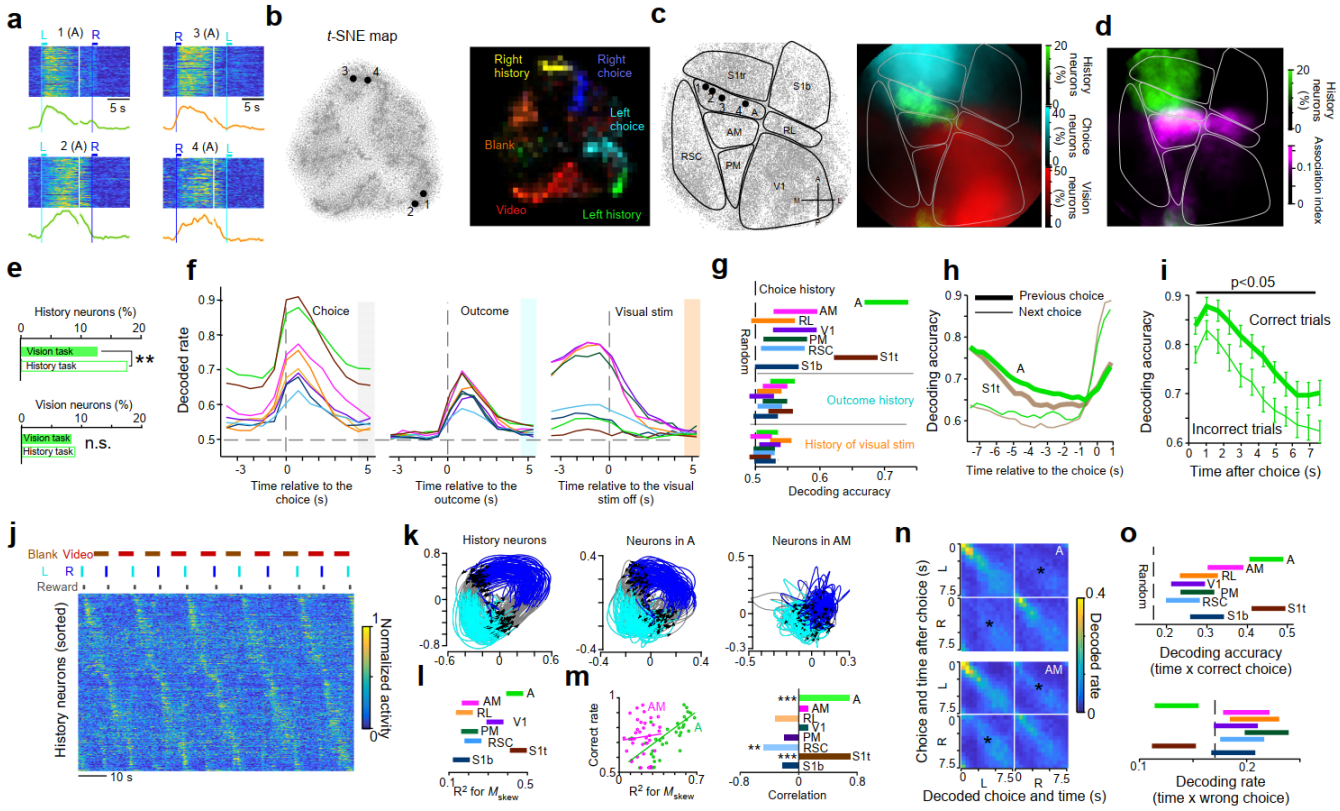

dynamics lead to behaviors that reflect past histories.

Figure 3. Robust representation of choice history in A. a. The representative history neurons. Number corresponds to that of panel **c. b.** The *t*-SNE result for the single neuron activity (left). Right panel shows that each cluster of *t*-SNE has the distinct functional types defined by the encoding model. **c.** Position of the single neurons imaged in history task (left) and the percentages of history, choice, and vision neurons. **d.** The percentage of history neuron and the association index was overlayed. Note that these two roughly corresponded to A and AM, respectively. **e.** Percentage of history neurons in A was higher in history task than vision task (top; $p=4.1 \times 10^{-4}$; chi-squared test). Percentage of the vision neuron in A was not different (bottom p=0.61; chi-squared test). **f.** Decoding accuracy of choice, outcome, and visual stimuli by activity of 20 neurons from each area before and after the choice onset, reward delivery, and end of the visual stimuli, respectively. Line colors corresponded to the areas shown in panel **g. g.** Decoding accuracy of the choice ($p=2.2 \times 10^{-13}$; one-way ANOVA), outcome (p=0.13; one-way ANOVA), and visual stimuli (p=0.094; one-way ANOVA) at the shaded time in the panel **f** were compared for each area. **h.** Decoding accuracy of previous choice (thick lines) and next choice (thin lines) as a function of the time relative to the next choice. Note that both A and S1t had larger information on the previous choice until 1 s before starting the next choice than next choice. **i.** The decoding accuracy of the next choice from A activity was significantly larger when the next choice was correct than when the next choice was incorrect (Wilcoxon signed-rank test with Bonferroni correction). **j.** The activity of simultaneously imaged history neurons was aligned by the peak time. The continuous sequential activity can be observed in the two consecutive trials. **k.** jPCA plot of the history neurons shown in panel **k** (right), that of A neurons (middle), and that of AM neurons (right). **l.** The R^2 of M_{skew} indicating how the rotational dynamics was dominant was compared ($p=5.1 \times 10^{-33}$; one-way ANOVA). **m.** The R^2 of M_{skew} was significantly positively correlated in A and S1t but not in AM (*** $p<10^{-6}$; ** $p<0.01$; *t*-test). **n.** Decoded rate of time after the choice using neurons in A (top) and AM (bottom). Note that cross-choice mistakes (*) were rare in A than AM. **o.** Decoding accuracy of the time with correct choice (top; $p=5.6 \times 10^{-14}$; one-way ANOVA) and decoding rate of the time with incorrect choice (bottom; $p=8.5 \times 10^{-10}$; one-way ANOVA). Error bars, mean ± s.e.m. in **i**, 95% confidence interval in **g, m,** and **o**.

4. Representation of posture

Neuronal activity in S1 typically represents simple somatosensory information, and thus the history neurons in S1t may be a consequence of habitual changes of the posture of the animal after making a choice in a trial. In this case, history neurons may not store the choice history internally, but they may simply reflect the posture of the mouse (Mimica, Dunn et al. 2018). To test this possibility, we analyzed the posture of the mice performing the tasks using a deep-learning based tracking method. We found that the angle of the tail was significantly different from the baseline values several seconds after the RP (**Supplementary Figure 5c**). Therefore, the position of the tail was useful information for the next choice in the history task. Overall, although the body was tightly restricted in the body-holder, mice still moved the tail and the paws related to the choice, the choice history, and the choice timing. Some parameters could potentially explain apparent task-related activities of neurons, which had been largely ignored in the previous studies.

We searched for relationships between the activity of neurons and these posture-related parameters during the history task. We constructed a linear model based on these parameters to fit the activity of each neuron during the history task in the same way as the encoding model for defining task-related neurons. In addition to forepaw position, tail position, and pupil size, we added a grooming behavior as a fitting parameter. We found that the neurons related to a tail, forepaws, and grooming were similarly distributed around the parietal cortex including S1 and A, while the pupil-size related neurons were mapped around visual areas (**Fig. 4a, Supplementary Figure 5e**), although pupil size and pupil size-related neurons would just respond to the luminance changes. A and S1 had a comparable ratio of neurons that were related to the tail and the paws.

We investigated whether the history neurons were related to the positions and/or movements of forepaws and a tail. Notably, 55.7%, 47.3% of history neurons were related to forepaws and tail, respectively. In total, 70.3% of history neurons were related to forepaws or tail. Since the posture and movements of the tail and the forepaws were related to the choice, this is not surprising. However, it remained unclear whether the activity of history neurons represented an internally stored choice history variable, or just reflected the sensory information that just happened to correlate with the choice on the next trial.

If neurons in A retain history information by receiving posture information, perturbing the posture information should decrease A's history information. To test this, we prevented the mouse from maintaining its posture during the ITI by randomly rotating the body holder (+24 or -24 degrees), forcibly introducing a physical disturbance making it difficult for the mouse to retain information of the previous choice by posture (**Fig. 4b**). Three mice successfully performed the task in this new condition. We mapped the neurons reflecting the angle of the holder ("**holder neurons**"; **Fig.4c**) and found that they had similar distributions as history neurons (n=3 mice, **Fig. 4d)**. Decoding analysis also showed the close relationship between history and posture information at the area level (**Fig. 4e**). By contrast, the representation of the angle and representation of the choice history was not correlated at the single neuron level (**Fig. 4f**). This result is evidence that the neurons regarding two different spatial features, the direction of choice and angle of the body, may share some neuronal resources in A and S1t, but the neurons process the information independently. Consistently, the percentage of history neurons and decoding accuracy of choice history were almost the same regardless of the holder movement in both A and AM (**Fig. 4g,h**). Thus, history neurons represent an internally stored choice history variable, independent of the posture. Taken together, history task and posture-perturbation experiments demonstrated that the most specific function of neurons in area A is storing choice history contributing to the next choice.

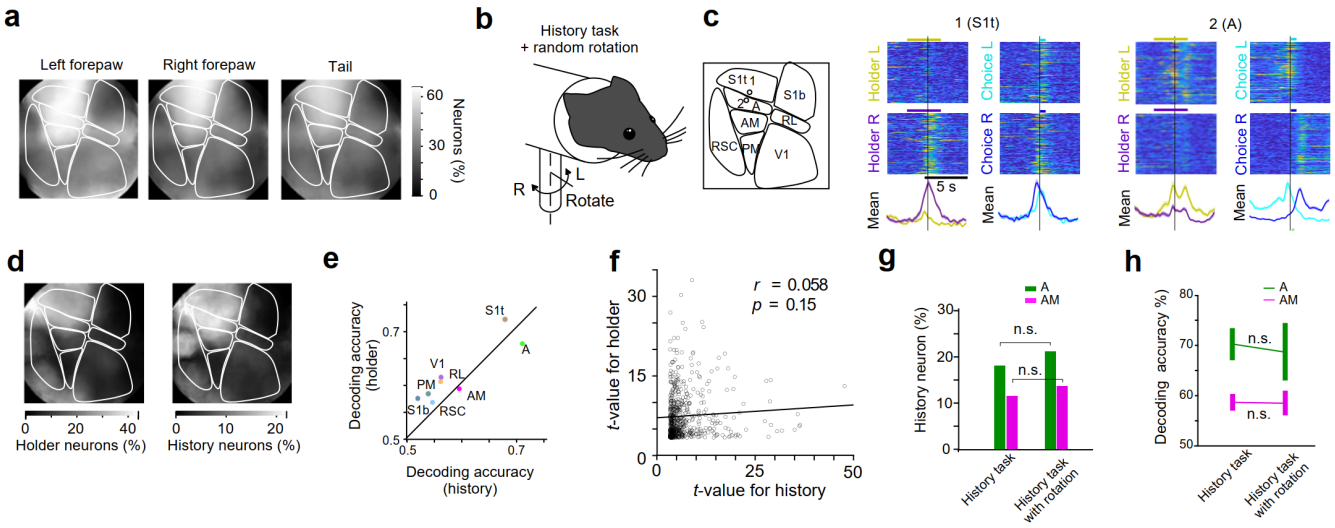

Figure 4. Posture related neurons and robust representation of the history neurons. a. The percentage of neurons that were significantly related to the left forepaw, right forepaw and the tail. **b.** A body holder was randomly rotated during the history task to prevent the mice from keeping choice history as the posture. **c**. Representative holder angle-related neurons. Number corresponds to the location in the left panel. Neuron 1 was holder-related but not for reward direction, whereas neuron 2 was related to both holder and reward. **d**. The percentage of history neurons and holder-related neurons. **e**. Decoding accuracy for the holder direction and the choice history in each area was compared. Note that the A and S1t had precise information for both. **f**. The t-values for the history-related activity and for the holder angle in each history neuron was plotted. No significant relationship was observed. **g**. The percentage of the history neurons in A (green) and AM (magenta) was not different between history task and that with random holder rotation (p=0.15 in A; p=0.38 in AM; chi-squared test). **h**. The decoding accuracy of choice history in A (green) and AM (magenta) was not significantly different regardless of the holder movements (p=0.87 in A; p=0.95 in AM; Wilcoxon's rank sum test).

5. Mesoscale correlation structure

PPC has anatomical connections with a variety of surrounding and remote areas (Hovde, Gianatti et al. 2018), but the functional correlation between those areas have not been extensively examined. In particular, based on the critical functional differences between A and AM that we found, A and AM may belong to distinct cortical networks that consist of different sets of densely interacting cortical areas. To address this question, we focused on the correlation in trial-to-trial variability, r_t. In the following, we analyzed r_t on two different levels: pairs of single-neuron activities and pairs of population activities.

First, to obtain r_t between a pair of single neurons, r_{t_single}, we averaged the activity of individual neurons over the sampling period by trial type, and subtracted this from the trial-wise activity. The trial types consisted of four sets of pairs of stimuli and responses, that is, the video stimulation and left choice, the video stimulation and right choice, the black screen and left choice, and the black screen and right choice. By this operation, we extracted the fluctuation components of single-neuron activity that are independent of the trial types. Correlation of these fluctuations were defined as r_{t_single}. The average value of r_{t_single} was small (~0.01) but larger than 0 even when the distance between neurons was more than 2 mm (**Fig. 5a**). Notably, a small number of pairs had a large positive correlation irrespective of distance (**Fig. 5b**). In fact, kurtosis (0 in the normal distribution) of correlation after Fisher's z-transformation was a very large value of 3.77 ($p < 10^{-6}$). Thus, we focused on neuron pairs with $r_{t_single} > 0.3$ (shaded areas in **Fig5b**) that were very rare in shuffled pairs in the following analysis to capture the dominant correlation structures.

In which regions are neurons tightly functionally coupled to neurons in AM and A? When mapping the "coupling" neurons in surrounding areas possessing r_{t_single} values > 0.3 with randomly chosen "seed" AM or A neurons, consistent spatial patterns emerged-(**"coupling neurons", Supplementary Figure 6a**). The coupling neurons were often localized in specific cortical regions. The localized region of the coupling neurons was S1t in most cases when the seed neurons were in A, while the region was variable when the

seed neurons were in AM (**Fig. 5c**). To quantify this property, we used the normalized spatial distribution of coupling neurons for each individual seed neuron of A or AM (**FIg. 5d**). Then we clustered these vectors using K-means (k=6) clustering and displayed the six mean vectors ("**preference vectors**") for each cluster. The result showed that interaction with most clusters from seed area A was largely dominated by S1t, while each cluster in AM preferred a specific area such as V1, RSC, A, and S1t (**Fig. 5e**). These relationships were observed in both vision and history tasks. Thus, AM had multiple interaction channels with surrounding areas, while A interacted with S1t, regardless of tasks. We quantified the similarities of preference vectors by averaging the angles between all pairs of the two vectors, and referred as "**coupling diversity**". We confirmed that the difference in the coupling diversity between A and AM is statistically significant by repeating K-means clustering with randomly chosen neurons in A or AM (**Fig. 5f**; **Methods**).

Is there relationship between the interarea interaction and functional types in the task? We termed the area where coupling neurons are located the "**preferred area**" and examined the relationship between the preferred area and task relevance. We found that both A and AM neurons with S1t in their preferred areas were significantly more likely to be choice and history neurons. Area A's neurons with visual areas (RL, V1, PM, or RSC) in their preferred areas were significantly likely to be vision neurons **(Fig. 5g).** Moreover, AM neurons preferring A had significant task relevance for all vision, choice, and history. Thus, A and AM neurons determined their functional types by interarea coupling at least in part.

Next, to investigate r_t of the population activity ($r_{t_population}$), we first reduced the dimension of population activity in each area into 10 by using PCA (principal component analysis) (**Supplementary Figure 6b,c**). Then, "fluctuation activity" was again calculated for each dimension by trial type similar to the single neuron case above, this time representing noise in population activation patterns. Then, we applied CCA (canonical correlation analysis) to each pair of areas and obtained an average of top 10 canonical correlation (CC_t) as $r_{t_population}$ The CC_t structure between areas was similar across task types (**Fig. 5h)** indicating that this structure reflects the underlying functional connectivity independent of the task. The CC_t between A and S1t was the largest among all the pairs (**Fig. 5h**), whereas when the CC_t was averaged across all connections for each area, A and AM had the largest and second largest CC_t, respectively **(Fig. 5i**). The dominance in CC_t in A and AM disappeared when the neurons with $r_{t,single}$ >0.3 were removed. Notably, the CC_t of AM and the other areas were uniform regardless of the paired areas across all 10 dimensions (**Fig. 5j**). Thus, area AM is an integration hub of interareal communication, whereas the A simply coupled with S1t, and such correlation structure at the population level critically depends on this subset of neurons.

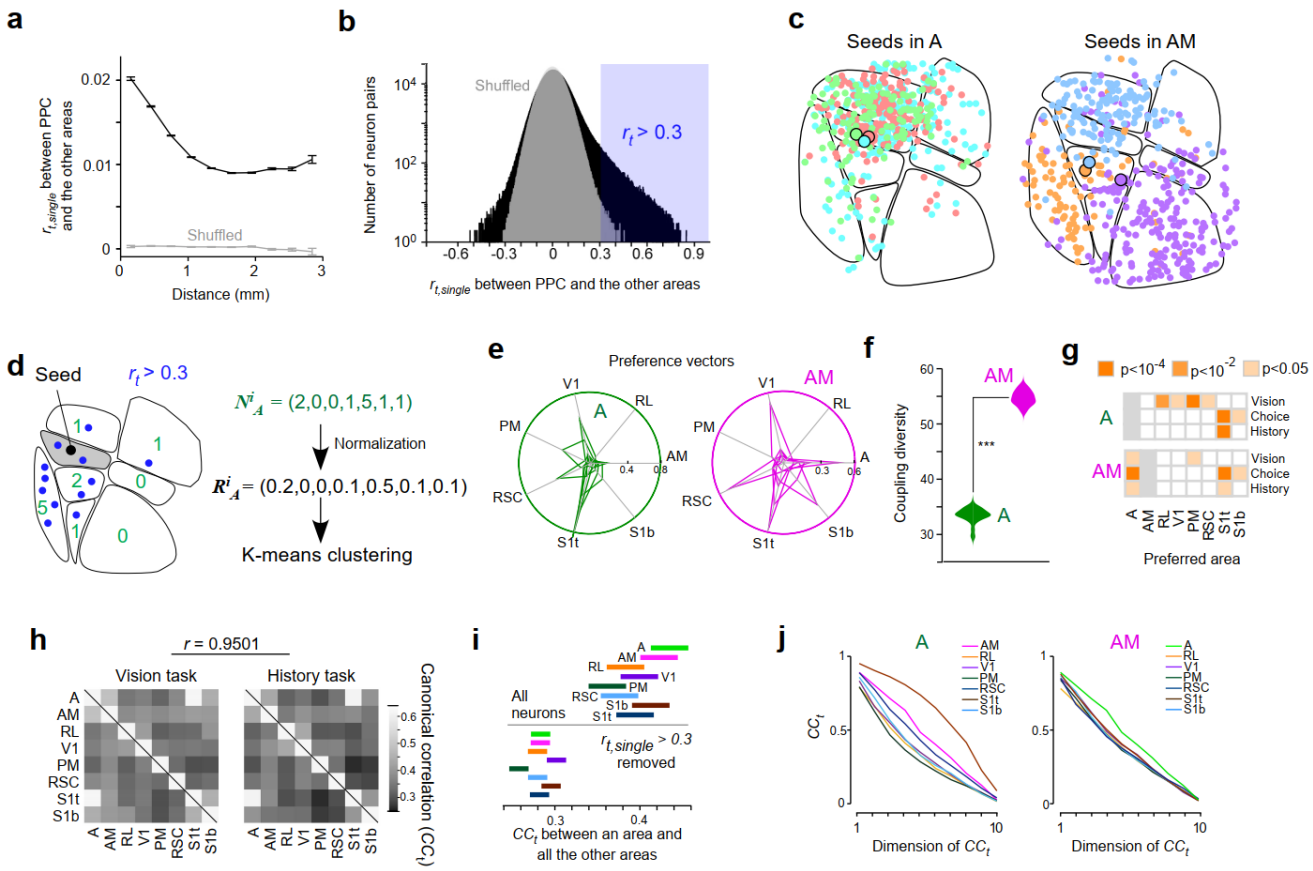

Figure 5. Mesoscale correlation of PPC and surrounding areas. **a**. Average of trial-to-trial correlation (r_{t_single}) between a PPC neuron and a neuron in the other areas was plotted against the distance between the neuron pair. The correlation was small but significantly larger than zero regardless of the distances. **b.** Log-scaled histogram of the r_{t_single}. The shaded area indicates a large positive correlation (> 0.3). **c**. The coupling neurons whose r_{t_single} with seed neurons (large circle) in A (left) and AM (right) were larger than 0.3 were shown with the same color as the seed neuron. Most neurons coupling to the A neurons were in the S1t, while the neurons coupling with the AM neurons were spreading but the spreading area was specific to each seed neuron. **d.** Schematic of the K-means (k=6) clustering of neurons in A based on the ratio vector, ***R***. This vector, given for each neuron, consists of the ratio of the number of coupling neurons (r_{t_single} >0.3) in the seven areas other than A. In this case, for example, R^i_A, the vector of the *i*-th neuron in A, had the largest value of 0.5 in the fifth element, which indicates this neuron had half the number of coupling neurons in the RSP. K-means clustering of the ratio vectors can identify the clusters of A neurons sharing the distribution of the highly correlated neurons. The analysis was done for all neurons in AM instead of A as well. **e.** Polar plots of the preference vectors of A (left) and AM (right). The preference vector is mean ratio vector of each cluster. **f.** Angles between any pair of the preference vectors which were obtained 1,000 times with randomly selected neurons. **g.** The relationship between the preferred area of single neurons in A or AM and their task-relatedness was compared. For example, significantly large number of A neurons preferentially coupling with the S1t neurons were choice neurons or history neurons whereas those coupling with the AM neurons were vision neurons. **h.** CC_t between pairs of eight areas during vision task and history task was highly correlated (r=0.95). **i.** The CC_t between an area to the other areas were compared. A and AM had the two largest CC_t (top; p=1.7 ×10^{-6}; one-way ANOVA), which was not the case when coupling neurons were eliminated (bottom; p=6.7 × 10^{-7}; one-way ANOVA). **j.** CC_t as a function of its dimension. CC_t from AM were uniform regardless of the interacting areas whereas A had large CC_t with S1t. Error bars, 95% confidence interval.

6. Relationship between mesoscale functional correlation and anatomical connections

Next, we asked whether distinct network level interaction of A and AM can be seen in the neuropil activity level observed in the same two-photon calcium imaging data. We examined the correlation of trial-to-trial "fluctuations" in neuropil activity ($r_{t_neuropil}$). The fluctuation of the neuropil activity was often localized in a specific area or a set of areas (**Fig. 6a**). Consistently, the K-means clustering revealed that the cluster boundaries of the neuropil activity approximately corresponded to the area boundaries (**Fig. 6b**). $r_{t_neuropil}$ was

similar regardless of the task types (**Fig. 6c**), so we combined these data for the following analysis. The neuropil activity in AM well correlated with PM, RSC, V1, RL, and A, whereas that of A highly correlated with S1t (**Fig. 6d**). The neuropil activity is known to reflect the local average of input in the imaged location (Kerr, Greenberg et al. 2005). Indeed, the trial-to-trial variation of a neuropil activity could be approximated by the average of 1,000 -10,000 neurons within several hundred micrometers from the center (**Supplementary Figure 7**). These data indicate that the correlation structures of average activity of neurons differs between A and AM.

Next, we utilized Allen connectivity atlas where the mesoscale connectivity between cortical and subcortical areas are comprehensively described. We used results of the anterograde tracer experiments where the adeno associated virus that delivers the fluorescent protein was injected in cortex or thalamus. We found that among cortico-cortical interactions only S1t clearly projected to A more than AM, whereas visual cortices (V1, AL, PM) and frontal cortices (orbitofrontal cortex, dorsal and ventral anterior cingulate cortex) preferentially projected to AM rather than to A (**Supplementary Figure 8a**). These data are consistent with our results that A represented sensorimotor parameters together with the S1t, and that AM is an interaction hub which was revealed by the mesoscale correlation analysis.

Does the correlation structure of the anatomical connections reflect the functional correlation? To address this question, we used the Allen connectivity data to quantify the degree of anatomical input similarity between any two regions as a correlation ($r_{anatomy}$, **Fig. 6e; Supplementary Figure 8b-d**). Interarea correlation between the anatomical input correlation and the neuropil correlation was surprisingly high (r = 0.94, **Fig. 6f,g**).The seed analysis reveals that the A and AM has distinct patterns of anatomical input (**Fig. 6h**) and the patterns highly resembled the neuropil correlations seen earlier (**Fig.6d**). These correspondences were the case regardless of the seed areas (**Supplementary Figure 8e**). This high correlation was more evident when both the cortico-cortical and thalamo-cortical projection data were combined (**Fig 6i**).Thus, $r_{t_neuropil}$, which reflects correlation of the average activity of neurons is strictly determined by $r_{anatomy}$. Taken together, these data suggest that the distinction of interarea communication in A and AM is led by the cortico-cortical and thalamo-cortical inputs.

Can the anatomical input correlation predict the correlation between population activities? The correlation between CC_t and $r_{anatomy}$ was moderate (r = 0.60, **Fig. 6j**). This moderate correlation did not change when the coupling neurons were eliminated (r = 0.61). Interestingly, the largest canonical component was the most unpredictable from the anatomical data (**Fig. 6k**). Thus, the canonical correlation analysis adds important information in population dynamics of neurons which is unpredictable by our analysis on the anatomical input correlation.

The correlation between cortical areas can be affected by the globally shared activity reflecting brain states or neuromodulator levels. To evaluate the contribution of global activity on the canonical correlation between areas, we first compared the canonical coefficient vectors (CCV). We found that the first CCV had a similar orientation, regardless of the paired areas (**Fig.6l**). This indicates that the largest components of correlated activity in CCA analysis is globally shared fluctuation. We also directly evaluated the correlated activity components across all 8 areas with generalized canonical correlation analysis. The first CCV also had a similar orientation to the first generalized canonical coefficient vector (GCCV) (**Fig. 6m**). These results indicate that the 1st canonical component reflects a global correlation across all cortical areas imaged. Such global correlation may be caused by factors other than the corticocortical or the thalamocortical inputs. We also confirmed the robustness of these results by repeating analyses only with 40% highly active neurons after denoising with non-negative deconvolution (36828 out of 91397 neurons; **Supplementary Figure 9**).

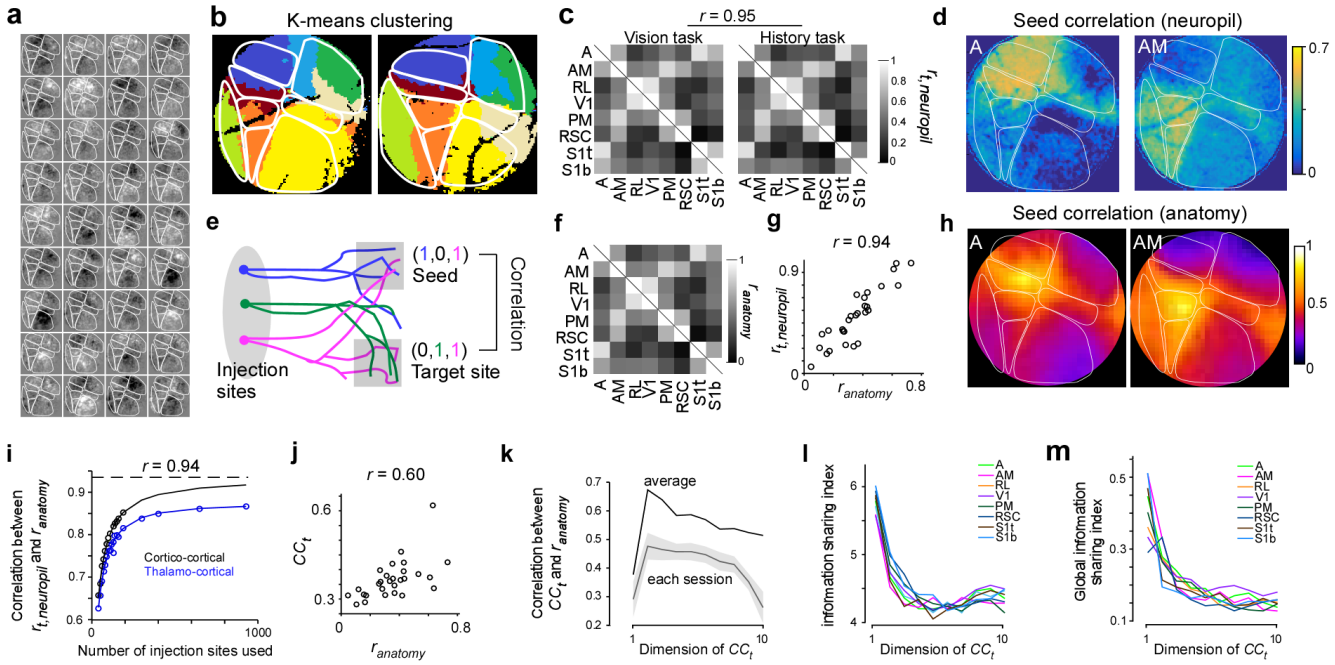

Figure 6. Comparison of functional and anatomical correlation structures.
a. Trial-to-trial fluctuation of neuropile activity of the mouse 2. Only the trials presenting the natural video and when the left choice was made were shown. Average neuropile activity of the all trials was subtracted from the activity of each trial. **b.** K-means clustering of each background pixels (k=8) from two mice resembling the functionally defined areas were shown. **c.** Correlation between background trial-to-trial activity ($r_{t,neuropil}$) in pairs of areas was very similar regardless of the task types (r=0.95). **d.** Seed correlation analysis of neuropil activity for A and AM. **e.** Anatomical input correlation ($r_{anatomy}$) was calculated between seed regions and target regions. This correlation indicates the extent which the two regions commonly receive the axonal projections from the other areas. **f.** $r_{anatomy}$ between each one of the pairs of 8 areas. **g.** $r_{anatomy}$ precisely predict $r_{t,neuropil}$. **h.** $r_{anatomy}$ map when the seed is in AI and in AM. Note that these maps resemble panel **d**. **j.** Moderate correlation between $r_{anatomy}$ and CC_t (r=0.60). **k.** The first (largest) CC_t component was the most inconsistent with the anatomical data. **l**. Information sharing index was plotted against the dimension of CC_t. The first component had the largest information sharing index for all areas. **m.** Global information sharing index was plotted against the dimension of CC_t. The first component had the largest global information sharing index for all areas. Error bars, mean ± s.e.m.

Discussion

In this study, we functionally characterized neurons in areas A and AM, two components of mouse PPC. Imaging during a vision-guided task revealed that neurons in area A showed choice-related activity, while neurons in area AM represented both the choice and visual information. Imaging during a history-guided task demonstrated that area A robustly represented choice history with choice-specific activity dynamics. Area A also represented the body posture of the mouse, cooperatively with area S1t. Experiments with perturbation of posture suggested that the choice history-related neurons in A and S1t stored a working memory for the upcoming choice. Analysis of the correlation of trial-to-trial variability indicated that, regardless of the tasks, the interactions of neurons in areas A and S1t were always large and stable, while the interactions of neurons in area AM and the surrounding areas were widespread and shared information specific to each area. These results were consistent with the patterns of corticocortical connections, revealed by both functional and anatomical data. Overall, we determined the functional differences of two PPC regions, areas A and AM, and characterized their distinct mesoscale interactions.

The functional differences along the rostrocaudal axis within the medial PPC suggests that various other PPC functions reported previously in mice would be mapped somewhere in this region. Neurons representing decision making, action history, and the posture should have been primarily observed within area A rather than area AM, because area A neurons were found to be activated by multiple somatosensory stimuli, choice, choice history, and body posture. On the other hand, in the vision-guided tasks, the neurons in AM would have more fundamental roles in the integration of visual information for coordinating behavior, compared to neurons in A. Note that RSC had few neurons with selectivity relevant to the tasks in this study, which suggests that selective activity in RSC may emerge only when mice engage in navigation (Minderer, Brown et al. 2019) or when the mice need to assess the value of an action (Hattori, Danskin et al. 2019). When vision is critical for choice during navigation and/or determining the value of an action, the neurons in A, AM, and RSC may cooperatively interact (Minderer, Brown et al. 2019). Fine functional segregation could also depend on task difficulty and learning stage (Driscoll, Pettit et al. 2017). However, even when the apparent functional representations are mixed, it is essential to precisely map the PPC subregions to see whether the mixed representation can be decomposed into several groups, each of which is mapped in a discrete subregion.

The differences in forms of interareal interaction among neurons in A and AM implies that AM has a more central role in integrating multimodal information, while A is more specific to controlling and/or monitoring behavior. In fact, area AM interacted with many areas through multiple independent channels, as shown in the correlation analysis, at both the single neuron level and the population level. Neurons in area AM may represent multiple types of information in a category-free manner, and thereby its microcircuit, or downstream circuit, could associate them when needed (Raposo, Kaufman et al. 2014). The long-range projections from various cortical areas including frontal cortex, such as the orbitofrontal cortex and anterior cingulate cortex, converged on the AM (**Supplementary Figure 8a**), supporting the view that AM is a key component in integrative, cognitive roles. Neurons in area A had relatively limited variation in long-range anatomical input, but they had much larger behavior-related activity cooperating with area S1. Thus, our results provide a new framework regarding PPC functions: first, a hub of widespread cortico-cortical interactions (area AM) and second, a core for behavior monitoring and control (area A) in PPC.

There is another new aspect of PPC function in mice that we present here: the representation of posterior S1 next to the anterior border of PPC. We found clear somatotopic organization was a critical difference between these two areas. By precisely mapping the borders of PPC and S1, we found that S1t and anterior part of PPC, area A, possessed almost the same rate of neurons representing choice, choice history and posture, even when posture perturbation was added during the task. Direct functional interaction between S1t and A, and/or top-down input from other areas may support the robust representation of history information in these parietal areas. Area A may send behavior-relevant information to S1 to modulate sensory processing as indicated in the top-down effects from secondary motor and somatosenroy areas to S1 (Manita,

Suzuki et al. 2015, Kwon, Yang et al. 2016). On the other hand, representation of the task-independent posture signals suggests that S1 sends the sensory signals to A. Thus, A and S1 would ordinarily send information bidirectionally. These results largely affect the interpretation of the activity of neurons in the parietal cortex especially on head-fixed navigation tasks (Harvey, Coen et al. 2012, Funamizu, Kuhn et al. 2016, Driscoll, Pettit et al. 2017, Krumin, Lee et al. 2018, Minderer, Brown et al. 2019) since the mice always need to coordinate the somatosensory information to maintain body balance during the tasks.

Our data also provided neuropil activity, which may be comparable to the data obtained with widefield, 1-photon calcium imaging data, without a single neuron resolution (Allen, Kauvar et al. 2017). The correlation of trial-to-trial fluctuation of the neuropil activity revealed a clear correspondence to the mesoscale anatomical structures. This correspondence was independent of the tasks and was also seen during passive viewing trials (**Supplementary Figure 8e**). These results imply that the shared input from distant areas shapes the spatial structure of cortical activity in general. In other words, the shared input in mesoscale connectivity could predict the brain-wide correlation structures of the functional fluctuations. We also estimated that the neuropil activity approximates the activity of thousands of neurons around the region, which implies that the mesoscale anatomical connectivity constrains the relationship between activities of two populations of neurons in connected cortical areas. Thus, the anatomical structures determine the mesoscale functional interaction, and thereby constrain the total activity of local individual neurons. This multiscale interaction would work as an effective constraint when simulating large-scale neural network models (Einevoll, Destexhe et al. 2019).

We found that the largest component of canonical correlation reflects globally shared information, and that this component is not well explained by anatomical data. The large influence of the global component implies that even to understand the relationship between two areas, it is necessary to consider their relationship to other areas or to the entire brain. This global component may involve neuromodulators reflecting states of arousal or motivation (McGinley, Vinck et al. 2015), slow rhythms that propagate throughout the brain (Neske 2015), neuronal activity related to movement (Stringer, Pachitariu et al. 2019), glial cell activity (Rasmussen, Asiminas et al. 2023), or combinations thereof.

Why are there two different functional modules in the medial PPC, areas AM and A? One possibility is that AM explores potential relationships between various signals from a number of cortical areas and their outcomes. When AM finds information important to the current situation, then neurons in area A store that information for a few seconds and contributes to the action, or behavior. Thus, area AM must constantly compare various pieces of information unbiasedly, whereas area A must focus on specific information. Such a fundamental difference in the required information processing may separate area AM and A into different functional networks. The coordination of the two would then create a unique and essential role for animals to survive in an ever-changing world.

Funding
This work was supported by the NIH (R01EY024294, RF1NS121919, and R01NS091335 to SLS), the NSF (1934288, 1707287, and 1450824 to SLS), the Simons Foundation (SCGB325407 to SLS), and the McKnight Foundation (SLS); RH was supported by fellowships from Naitoh Foundation and JSPS, JP22wm0525007 from AMED, and JP22H02731 and JP21H05135 from MEXT/JSPS; JNS was supported by a career award from Burroughs Welcome; LBT was supported by Weatherstone Predoctoral Fellowship (#9630) from Autism Speaks, an NIH NRSA award (F31HD084174), an NIH training grant (T32NS007431), and the HHMI Graduate Training Program in Translational Medicine at UNC-Chapel Hill.

Conflicts of interest
SLS consults on multiphoton optics. SLS and CHY have interest in the company Pacific Optica. There are no other conflicts of interest.

Author contributions
RH designed and performed most experiments and analysis, and developed and built specialized behavior rigs for this study. LBT performed the experiments measuring cortical area locations both functionally and registered to stereotaxic coordinates. ITS provided training and supervision for imaging experiments. CHY and JNS provided technical assistance with large field-of-view two-photon calcium imaging. SLS assisted in the design of experiments and analysis, and supervised all aspects of the work. RH and SLS wrote the paper.

Acknowledgements
The authors thank J. Canzano for helpful comments on the manuscript.

Methods

Subjects

All procedures were reviewed and approved by the Institutional Animal Care and Use Committee (IACUC) of the University of North Carolina at Chapel Hill, which ensures compliance with the standards of the American Association for Laboratory Animal Science (AALAS). Mice were imaged at the age of 8-40 weeks. Adult C57BL/6J mice (Jackson labs) or GCaMP6s (Chen, Wardill et al. 2013) expressing transgenic adult mice of both sex were used in this study. GCaMP6s expressing were induced by the triple crossing of TITL-GCaMP6s line (Allen Institute Ai94), Emx1-Cre line (Jackson Labs #005628) and ROSA:LNL:tTA line (Jackson Labs #011008) (Madisen, Garner et al. 2015). Intrinsic signal of equal numbers of males and females C57BL/6J mice were imaged for the P60 and P100 groups (6 mice per time point, 3 of each sex for each time point) when the variability of the visual areas was examined.

Surgical procedure and experimental steps for intrinsic imaging

On the day of imaging, anesthesia was induced with 5% isoflurane. After initial anesthesia induction, 2.5 mg/kg chlorprothixene was administered via intraperitoneal injection. Isoflurane was reduced and maintained between 1-2.5% during surgery. Ophthalmic ointment (Lacri-lube, Allergan) was applied to both eyes and a heating-pad maintained body temperature. The scalp was then resected, exposing the skull over visual cortex. To register functional maps of visual cortical areas to stereotaxic landmarks, three reference points were labeled with a marker near primary visual cortex (0.8 mm anterior to lambdoid suture, 2.3 mm lateral to the midline). Using digital calipers, three separate measurements were taken from the center of each dot to midline (mediolateral coordinates) and from the center of each dot to the lambdoid suture (rostrocaudal coordinates). For each reference point, the three measurements were averaged. We used the lambdoid suture instead of bregma as a landmark since the position of the bregma is less reliable to define the coordinates of the brain (Chan, Kovacevic et al. 2007, Spring, Lerch et al. 2007, Barth and Mody 2011). Although it lacks accuracy, one may be able to use the approximate distance between the lambdoid structure and bregma (~4.0 mm) to convert the coordinates from lambda-based to bregma-based one.

A head-plate was affixed to the skull. A 3.5-4 mm craniotomy was performed over the visual areas when needed. The glass window with 3 mm diameter was put onto the cortex, and a tissue adhesive was used to seal between the glass and the skull. Then, the mouse was transferred to the intrinsic signal optical imaging (ISOI) system. The ophthalmic ointment was removed from the contralateral eye prior to imaging by manually blinking the eye gently. Isoflurane was maintained between 1-1.5% during imaging. The camera was focused on the skull to acquire an image of the dots relative to the head-plate and major vessels visible through the skull. The camera was then adjusted for ISOI imaging and an initial retinotopy set was acquired through the skull (Kalatsky and Stryker 2003). After imaging experiments, the mouse was removed from the ISOI rig and given a second dose of 2.5 mg/kg chlorprothixene. The ophthalmic ointment was reapplied to the contralateral eye.

Intrinsic imaging and sensory stimuli

The brain was illuminated with 700 nm light and imaged with a tandem lens macroscope focused 600 μm into the brain from the vasculature. Images were acquired with a 12-bit CCD camera (Dalsa 1M30), frame grabber and custom software (David Ferster, with in-house modifications by Jeffrey Stirman & R. H.) at 30 frames per second. Visual stimuli were presented to the left eye relative to the imaged hemisphere using a Dell LCD monitor (Dell U2711b, 2560 x 1440 pixels, 60 Hz) sitting 20 cm from the mouse. The monitor was tilted towards the mouse 17.5° from vertical to cover the visual field (110° by 75°). All stimuli were generated and presented using MATLAB and Psychtoolbox (http://psychtoolbox.org/) (Brainard 1997, Kleiner, Brainard et al. 2007). All stimuli were modified to correct for visual distortions caused by the flatness of the monitor. Retinotopy was initially mapped by showing the animal a single, square-wave white bar drifting across a black background to identify right V1 and right HVAs (horizontally for azimuth and vertically for elevation). This stimulus was presented for 30 – 50 eight-second-long cycles.

For auditory stimuli, a standard computer speaker was placed at either back of the mouse or left side from the mouse. Speaker was located approximately 10 cm from the mouse. The speaker was controlled with the custom-written LabVIEW software. Auditory stimuli were always 800 ms white noise bursts every 8 seconds. For somatosensory stimuli, the vibration of the membrane of the same speaker was used. The speaker was controlled with the same LabVIEW software. One side of a plastic pipette was attached to the membrane with tape, and the other side of the pipette was attached to a body part (tail, trunk, neck, left pinna, left whisker pad, left forelimb and left hind limb) gently with a tape. As a result, the vibration of the speaker membrane was transferred to the body. Fifty Hz pure tone which gives a 50 Hz sinusoidal movement of the membrane for 0.8 sec vibrated the skin of the targeted body part without sound every 8 seconds. Both cutaneous and proprioceptive responses would be obtained by these stimuli. The speaker sound of 50 Hz tone is far from mouse hearing range (Engle and Barnes 2012), and we confirmed that the stimulation did not evoke the activity in the auditory areas with ISOI mapping. The room light was turned off when a pinna or a whisker pad was stimulated to prevent the pipette from being seen since the vibrating pipette was just in front of the left eye. The pipette was outside the visual field from the mouse eyes when the tail, trunk, neck, left forelimb and left hind limb was stimulated.

Analysis of ISOI data

The images with 12-bit pixel data were binned in software four times temporally and 2 x 2 spatially, resulting in images with 16-bit pixel data. From these binned images, Fourier analysis of each pixel’s time course was used to extract the magnitude and phase of signal modulation at the stimulus frequency for mapping of visually evoked areas. The phase of signal modulation was used to generate maps of the phase of the cortical response, mapping retinotopy of the visual cortex. To identify the areas activated by auditory and somatosensory stimuli, mean intensity of each pixel for 2,000 ms after the stimulus onset was subtracted from mean intensity of the pixel for 1,000 ms before the stimulus onset across all stimulus trials. The negative value of the pixel implies the evoked activity in the pixel. The image with the evoked activity was filtered with Gaussian filter with a standard deviation of 10 pixels, and the pixel with minimal value was identified as a peak location (downward signal is observed in the activated area). The median value of all pixel was set to the baseline. The mean value of minimal value and baseline was set the threshold, and the pixels with less than the threshold were regarded as the evoked area.

Image registration for ISOI map

Retinotopic maps were drawn (ImageJ/Fiji) (Schindelin, Arganda-Carreras et al. 2012, Schneider, Rasband et al. 2012, Schindelin, Rueden et al. 2015) based on the first set of imaging data (obtained through the skull) and then modified as needed with the second set (obtained without the skull) to ensure that boundaries between cortical visual areas were accurately identified. These maps were drawn based on color reversals (Wang and Burkhalter 2007) and other landmarks present in the retinotopy data. For example, when identifying AL, we look for three stereotyped color reversals to identify the border between AL and LM/LI, AL and V1, and AL and RL. We also used the magnitude maps from these stimuli to ensure that the anterior boundary between AL and non-visual areas is accurately restricted to the area that is visually responsive.

The stereotaxic reference coordinates were first plotted, and the registered to the cortical area location by aligning the plotted coordinates with the reference image (image of the stereotaxic reference coordinates marked on the skull). The reference image was then scaled such that 1 mm in the reference image was the equivalent of 1 mm in the coordinate plot. The reference image was then rotated and moved in X-Y (rigid transform) so that the plotted stereotaxic reference coordinates were in agreement with the marks in the reference image. Using the plotted stereotaxic reference markers, the same image transformations were applied to the retinotopically identified ROIs, producing a set of ROIs registered relative to stereotaxic reference coordinates. This was done for each mouse in the data set. The center of mass for each ROI was computed, and this was then converted to millimeters by measuring the number of pixels in 1 mm and dividing the center location by the conversion factor.

Functional definitions of cortical areas

Previous studies on the demarcation of HVAs based on the anatomical tracers have shown that the HVAs comprised AL, RL, A, AM, PM, LM, LI and posterior areas (Wang and Burkhalter 2007). With functional mapping with ISOI, we and other laboratories have identified comparable areas with the definition based on the anatomical tracing, but the definition of area A and RL has not been not consistent between studies. In this paper, we simply followed our previous studies (Stirman, Smith et al. 2016, Smith, Townsend et al. 2017, Yu, Stirman et al. 2018) on the definition of HVAs (AL, RL, AM, PM, LM, and LI) for HVA mapping (**Supplementary Figure 1**) with ISOI.

In the analysis with two-photon imaging, since we found that area A largely lacked the retinotopy, we redefined the areas as follows. By data from two-photon calcium imaging (tactile stimuli and visual stimuli), first, the V1, AM, S1t, and S1barrel were determined by the retinotopic and somatotopic organizations. When the cortical neurons activated by visual and tactile stimuli were overlaid, we found an area where the evoked activity was almost absent in the medial space of the FOV. The area was determined as RSC. Then, the triangle behind AM between RSC and V1 was determined as PM. Then, the rectangular space between the S1 barrel and V1, and between S1t and AM was determined as RL and A, respectively. We found a borderline between S1t and S1 barrel, a borderline between V1 and AM, and a borderline between V1 and PM lined up in the straight line. We used the line for the border between RL and A. These definitions are largely consistent with the previous anatomical definitions of the Allen Mouse Brain Common Coordinate Framework (CCFv3) (Wang, Ding et al. 2020). We did not discriminate the RSPagl and RSPd in this study since we did not find any functional landmarks. When we analyzed the differences or interactions between areas, we picked up the neurons in each area excluding the neurons in a 50 μm-wide transition zone, to avoid contamination.

Surgical procedure for head-fixed behavior

Mice were anesthetized with isoflurane (1.5 – 1.8%) and acepromazine (1.5 – 1.8 mg/kg body weight) when performing craniotomy over the posterior parietal cortex. Carprofen (5 mg/kg body weight) was administered prior to surgery. Mice body temperature were maintained using physically activated heat packs during surgery. Mouse eyes were kept moist with ointment during surgery. The scalp overlying the dorsal cortex was removed, and a custom head-fixing imaging chamber ((Hira, Ohkubo et al. 2013); **Supplementary Figure 3b**) was mounted to the skull with a self-cure dental adhesive system (Super bond, L-Type Radiopaque; Sun Medical) and luting cement (Micron Luting; PD). The surface of the intact skull was subsequently coated with clear acrylic dental resin (Super bond, Polymer clear; Sun Medical) to prevent drying. Mice were then returned to their cages.

After the behavior training and before the two-photon imaging sessions, a second surgery was done with the same anesthetic conditions described above. A 4-mm diameter craniotomy was performed over the posterior parietal cortex (right hemisphere, centered 2.0 mm lateral and 2.50 mm posterior from bregma) and covered with two #1 thickness coverslips with 3.5 mm diameter and one #1 thickness coverslip with 5 mm diameter, glued together with optical adhesive (NOA68, Norland). The edge of the upper coverslip with 5 mm diameter was sealed with luting cement (Micron Luting; PD). Mice were then returned to their cages. The condition of the cortical surface was typically the worst in the first week but recovered after the second week. We did not image the activity of neurons when the cortical surface above the PPC was not clear.

Head-fixed tasks

In all tasks, mice were kept in a body-holder fixing the head to the stage (**Supplementary Figure 3a,b**). A white square in the left or right position at the display was presented when the mouse licked to the left or right (**Supplementary Figure 3c**). This feedback was given to allow mice to understand that the licking left and licking right are critically different actions in these tasks.

In the visually guided task (vision task or "V" task, **Fig. 2a-c**), mice had to lick left or right based on the visual stimuli presented in the display located at the left visual field of them. On the trials, a natural video taken in the cage was presented mouse had to lick left after 4-s sampling period to get a drop of water as a reward (1.5 - 2.0 μl) from the left lick port. On the trials a black screen was shown in the display, the mice had to lick right to get the reward from the right lick port. During the sampling period, the lick-ports were withdrawn. Mice learned to not lick during this sampling period (**Supplementary Figure 3f,g**). The visual stimuli were also presented during the response period and 2 s after the response when the response was correct. The visual stimuli stopped when the response was incorrect. During the inter-trial-interval (ITI), a gray screen was presented. In the vision task, the probability that correct direction is left was #R / (#L + #R), where #L and #R is the total number of correct choices in left and right trials before the trial in the session, respectively. When the mice were rewarded three times in the same direction, the correct direction was switched on the next trial. These procedures were made to avoid biased licking in the same direction.

We also designed a choice history-dependent task (history task or "H" task) with the same set up as the vision task. In this task, the mice had to choose the other side of the choice of the previous trial (**Fig. 3a**). Thus, the information of direction of the previous choice had to be stored for 6-10 s from the previous choice to the next choice including ITI (2 – 6 s) and sampling period (4 s). Since the visual stimuli were randomly presented during the sampling period, the mice had to ignore the visual stimuli.

In some sessions of the choice history-dependent task, the body-holder was moved randomly to prevent the mice from storing information of the previous trials in the body-angle. In every trial, the body-holder was reset at the center position when the ITI started and then moved to either left or right angle (± 24 degrees).

For training sessions before the vision task and history task, we trained the mice with "V+H" task, where the mice can follow either the visual stimuli and history of the choice. In this task, the correct chosen direction was the opposite of the previous choice as in the history task, and the visual stimuli were consistent with the correct direction. In a few other sessions of history tasks, the display was switched off or the body-holder was randomly moved in the dark environment. We conducted but did not analyze the data of two-photon imaging during the V+H task, the history task in the dark, or the history task in the dark with body-holder movements in this study.

Training of the tasks

We trained the mice with a serial schedule (**Supplementary Figure 3d**) in custom-made training boxes or under the microscope. After recovery from the surgery of a headplate attachment to the skull, we started water restriction (1 ml / day) until the weight was 85 – 90% of the original weight. Then, we started to train the mice with "pre-training". At the first day of pre-training, the mice freely got a drop of water from both left and right licking ports with the head-fixed condition for 30 min. During the pre-training after the second session, the temporal pattern of the task (i.e. SP (sampling period), RP (response period) and ITI (inter-trial-interval)) was introduced as the vision task described above except for that the RP was unlimited. In other words, the incorrect licking did not result in the termination of RP so that the mice could try to lick until they lick to the correct direction and get a drop of water (1.5 - 2.0 μl). The visual stimuli were switched at every trial between a natural video and a black screen, and the correct licking directions were left and right, respectively as in the V+H task. The distance between the two licking ports was set relatively small (~2 – 4 mm) to allow the mice to find both spouts easily and was gradually increased up to ~5.5 mm (distance depended on the mice). The experimenter assisted the mice to find the licking port when the mice missed it for several minutes by repositioning it and manual delivery of water. Overall, the pre-training was used to make the mice learn to lick both sides of the licking ports, which took 2 – 5 sessions. When the number of reward mice got exceeded 150 per session (< 2 hours), the task was switched to the V+H task. In this task, the temporal pattern of the task was the same as the vision task, but the correct direction of licking was set the opposite side of the previous direction. Therefore, the mice could either follow visual stimulus or the choice history to get the reward. The experimenter assisted the mice to find the licking port by repositioning the spouts and manual delivery of water when the mice lost motivation, especially in several initial sessions. The V+H task was

trained to give the baseline condition where we can retrain the V task and H task from the task. After the acquisition of the V+H task, we switched the task to the vision task. The correct rate immediately dropped after switching from V+H task to V task but recovered after that. The transient decrease in the correct rate indicates that the mice used history information during the V+H task. After reaching the criteria, the mice were trained to perform the task under the microscope. Two out of three mice reached the criteria also under the microscope during two-photon imaging (black dots in **Supplementary Figure 3e**), but mouse 3 did not. After the V task, we retrained mice with V+H task to recover the baseline condition. After that, we switched the task to the H task. We found that the correct rate dropped immediately after switching the task from V+H task to H task and recovered again. This transient drop demonstrates that the mice also used vision information in the V+H task. In the H task, all the mice reached the criteria under the microscope during two-photon imaging (blue dots in **Supplementary Figure 3e**). With two out of three mice, we trained the H task with randomly moving body-holder, and both mice reached the criteria during the two-photon imaging (orange dots in **Supplementary Figure 3e**). Throughout the training, mice kept their weight more than 85 % of the original weight and were monitored their health conditions every day for about 4 months.

Two-photon imaging

Two-photon imaging was carried out using custom Diesel2p microscope controlled by costume LabVIEW software (National instruments). Two-photon excitation laser from an 80-MHz Newport Spectra-Physics Mai Tai DeepSee was scanned by a resonant scanner (CRS 8 KHz, Cambridge Technologies), and two Galvo scanners (62010H, Cambridge Technologies). Photon signal was collected by PMT (H7422P-40, Hamamatsu) and amplified with a variable high speed current amplifier (#59-179, Edmund Optics). Two-photon imaging of 3 x 3 mm^2 was collected at 5.6 Hz for imaging. Since the maximum scan angle of the resonant scanner is limited, we made two rectangles with 1.5 x 3 mm^2 to cover 3 x 3 mm^2 FOV (**Supplementary Figure 2a,b**). With these parameters, a neuron with a 10 μm diameter circle was supposed to have 29 pixels inside the ROI (region of interest), including more than 100 laser pulses on average **(Supplementary Figure 2c)**. Imaging was performed with <120 mW excitation 910 nm laser out of the front of the custom-made objective lens (0.55 NA). Mice were head-fixed at about 15 cm from a flat monitor, with their left eye facing the display during imaging. An 80° x 45° the left visual field was covered with the display. During imaging, we monitored a diameter and position of left pupil, movements of whiskers, both forelimbs, a mouth and a tail with four custom-controlled CMOS cameras at 30 fps. Licking to the left or right licking port was also monitored with an electrical circuit (Slotnick 2009). The timing signals for resonant scanner were used for synchronization of all the other devices and the data. The imaging depth below the dura was between 80 μm and 180 μm (layer 2/3). To ensure the scanning planes are parallel between different sessions, we tilted the stage of the body holder manually before the imaging sessions to make the imaging plane horizontal to the surface of the brain.

Visual stimulation for retinotopic mapping was displayed on 60 Hz 7” LCD monitor (9.5 x 15 cm^2). A white vertical or horizontal bar was drifted from temporal to nasal or top to bottom at a cycle of 8 s. The tactile simulation for mapping of the somatotopic organization was made with a gentle and brief air-puff (20 – 50 ms) to a specified part of the body at a cycle of 4 or 8 s. Both visual and tactile stimuli were repeated at least 20 cycles. When the mouse started to actively move during the stimuli, the imaging was stopped and the data was discarded.

Image processing

Image analysis was performed using ImageJ (National Institutes of Health) and MATLAB (MathWorks, Natick, MA, USA) software. Image sequences were corrected for focal plane displacement, and region of interest (ROIs) within somata were automatically determined using suite2p (Pachitariu, Stringer et al. 2017). The fluorescence traces and shape of ROIs were inspected visually. Elongated ROIs are more likely to be dendrites or axons, so those with a ratio of the length of the major axis to the length of the minor axis greater than 3 were excluded. To eliminate the effect of background activity, we made a square-shaped mask whose

pixels were within 50 μm from the edge of the ROI, excluding pixels less than 5 pixels from the edge of the ROI and pixels within the other ROIs. Then, we subtracted the mean value of this area from the mean value of the ROI. The obtained value was referred to as "activity" of the neuron. Those neurons showing activity with skewness of > 0.3 (Hira, Ohkubo et al. 2013) were regarded as **"active neurons"** and used for analysis. We also obtained active neurons with kurtosis > 5 as and defined them as **"highly active neurons"**. Non-negative deconvolution was conducted with foopsi (Vogelstein, Packer et al. 2010). The values after non-negative deconvolution was thresholded with median + 1.5 x 1.4826 x mad and was shown as the inferred spike. Trajectory of neuronal population activity was investigated with jPCA analysis (Churchland, Cunningham et al. 2012). jPCA is a method for finding linear combinations of principal components that capture rotational structure in the population activity. jPCA determines a skew-symmetric matrix, M_{skew}, that approximates the derivative of the population dynamics by the current population activity. R^2 for M_{skew} indicates quality of the fitting.

To analyze neuropil activity, the pixels within each ROI identified with suite2p was filled with each background activity described above. After that, the size of the image was reduced to 120 x 120 pixel^2, where the size of a single pixel is 25 x 25 μl^2.

Processing of video data using DeepLabCut

We recorded video data (160 x 120 pixel, 30 fps, ~ 1 hour / session) from three IR cameras (Basler SCA640-70GM, GIGE, Lens: Basler C125-1218-5M, 12 mm) put in front of the mouse, at the rear of the mouse, and in front of the left eye during the task performance. We analyzed these data with DeepLabCut (Mathis, Mamidanna et al. 2018) (https://github.com/AlexEMG/DeepLabCut) for tracking the left and right forepaws, the tail and the pupil. We labeled each body part in randomly extracted 100 frames from each video and trained a model for each video data for each session using the 100 labeled data. About 20,000 iterations were made in training the model. Google colaboratory was utilized for the training of the model using GPU. We further analyzed the positions of the body parts in frame with estimated relative likelihood was more than 0.9. The horizontal and vertical position was directly extracted from the result of the tracking, and then we obtained the direction (angle) of the left and right forepaws and the tail from the body center (**Supplementary Figure 5 a,b**). The pupil size was calculated by identified two edges of the left pupil (**Supplementary Figure 5d**). We visually inspected the quality of the results and confirmed that all the tracking results were as precise as the human vision.

Encoding models

To map the neurons encoding visual, choice and history-related information, we used a simple linear encoding model (**Supplementary Figure 4**). The activity of each neuron was fitted by a set of predictor variables for each session. The predictors consisted of the time bins (3 frames each, 11 bins) of the visual stimuli, chosen direction (left or right), past chosen direction (left or right), reward direction (left or right), and ITI (inter-trial-interval). To avoid picking up non-selective neurons, we added non-selective predictor variables. The Bonferroni-corrected *p*-values for the visual stimuli, choice and choice history parameters in the encoding model were used to identify the vision, choice, and choice history-related neurons, respectively. P-value ($p<0.001$) for each parameter of the regression model was used to determine the significance. The *t*-values in the regression model were used to map the strength and position of each task-related neuron. The same linear model with different parameters which are obtained from the video analysis was used to identify the neurons related to the posture, movements, and pupil diameter (**Supplementary Figure 5e**).

Decoding analysis

The direction of the choice was decoded by population activity of neurons with a logistic regression model (Matlab built-in function, "glmfit" with binomial distribution and logit link function). For each time bin, the model was trained to predict the chosen direction using the activity of neurons in the time bin except for the trial. Then, the choice in the trial was predicted by the activity of neurons in the trial (leave-one-out). The outcome

(reward or punishment) and visual stimulation (video or blank) was similarly decoded by the activity of neurons. The number of trials was matched to the smaller number of the right and left selections in order to align the number of selections between the left and right selections. For example, if the left selection had 150 trials and the right selection had 200 trials, all trials from the left selection were used and 150 trials from the right selection were randomly selected. To avoid bias due to the selection of trials, we repeated the random selection 20 times and averaged the 20 decoding results to determine the accuracy of the decoding. By this manipulation, decoding accuracy is 50% when the neuron has no information at all.
The time after the initiation of the videos (**Fig. 2k**), or the time after left or right choice (**Fig. 3f**) was independently decoded by using a support vector machine (Matlab built-in function, fitcsvm) and activity of neurons. For decoding the time after the video starts, each imaging frame (185 ms) during the sampling period was used as a label for classification of the time. For decoding the time after the choice, 9.5 seconds after the choice were divided into 17 parts (each part being 555 ms) and each part was used as a label for the classification. We trained multiple support vector machines, each of which classifies whether a given set of neural activities belongs to *i*th interval or not (i = 1, 2, ..., the total number of parts). A ten-fold cross-validation procedure was used to avoid over-fitting.

Correlation analysis at single neuron and population level

Correlation of trial-to-trial variance of activity between a pair of single neurons was defined as r_{t_single}. To calculate r_{t_single}, we averaged the activity of individual neurons over the sampling period, and the average across each trial type was subtracted from this value. The trial types consisted of four sets of pairs of stimuli and responses, that is, the video stimulation and left choice, the video stimulation and right choice, the black screen and left choice, and the black screen and right choice. By this operation, we extracted the fluctuating components of single-neuron activity that are independent of the trial types. We defined a neuron with 0.3 or more r_{t_single} with a neuron in AM or A as a coupling neuron if the neuron is not in the same area. We counted the number of coupling neurons in each area and considered the number as a vector. We normalized this vector so that the sum is 1 (ratio vector) only when the total number was 5 or more. Then we clustered the ratio vectors using K-means (k=6) clustering and defined the mean vector of each cluster as a "**preference vector"**. We averaged the angles between all pairs of the preference vectors, and referred as "**coupling diversity**". For comparison of coupling diversity of AM and A, we randomly extracted half of the ratio vectors from AM and A, conducted K-means clustering, and obtained the coupling diversity 1,000 times to know the distribution of the coupling diversities. We defined area X as the **"preferred area"** of a neuron in A and AM if the neuron had one or more coupling neurons in the area X. We then compared the proportion of task-related neurons (i.e., vision, choice or history neurons) between the neurons whose preferred area includes area X and the other neurons by a chi-square test.

To calculate the trial-to-trial fluctuations in neuropil activity ($r_{t_neuropil}$), we averaged the neuropil images over sampling period, and the average image across each trial type was subtracted from this image. The trial types consisted of four sets of pairs of stimuli and responses, that is, the video stimulation and left choice, the video stimulation and right choice, the black screen and left choice, and the black screen and right choice. By this operation, we extracted the fluctuating components of neuropil activity that are independent of the trial types.

CCA (canonical correlation analysis)

CCA was used to compare neural population activities in two areas. As a preprocessing step, the data from an area was reduced to N_{PCA} (=10) dimensions using PCA (principal component analysis). This ensured that CCA did not find dimensions of high correlation but low data variance (Sussillo, Churchland et al. 2015). To estimate the area-to-area correlation in the task-independent variables, the CCA was calculated in task-independent spaces, which is practically the same as noise correlation, as follows **(Supplementary Figure 6b)**.

Value of each principal component was averaged over 4-s sampling period in each trial. Then, we obtained the fluctuation component of the value by subtracting the mean of each four trial-types. Here four trial-types were defined by a combination of visual stimuli and choices: natural video and left choice, natural video, and right choice, black screen and left choice, and black screen and right choice. We call these fluctuating dimensions task-independent space. The fluctuation was concatenated into one column vector per a principal component (N_{PCA} by N_{trial} matrix, N_{trial} is a total number of four trial types). CCA between any pair of the cortical areas was obtained in these task-independent spaces. The N_{CCA} (=10) CCA values were averaged and the value was referred to as $CC_{t,X,Y}$, where X and Y is a cortical area.

We also used CCA to estimate the amount of shared information between an area and the other areas (**Fig. XX; Supplementary Figure XX**). Suppose we have time series of the N_{PCA} variables (principal components) in the task-independent spaces, **X** and $\mathbf{Y_a}$, from an area X and another area Y_a, respectively,

$$\mathbf{X} = (X_1, X_2, \ldots\ldots X_{N_{PCA}})',$$
$$\mathbf{Y_a} = (Y_{a,1}, Y_{a,2}, \ldots\ldots Y_{a,N_{PCA}})',$$

where X_i and $Y_{a,i}$ (i=1,2,3,… N_{PCA}) are column vectors, whose length is equal to the number of trials (N_{trial}). To calculate N_{CCA} canonical correlation values, linear transformation of **X** and $\mathbf{Y_a}$ with weight matrices (canonical coefficient vectors, CCVs) $\mathbf{A_a}$ and $\mathbf{B_a}$ give canonical scores, $\mathbf{S_a}$ and $\mathbf{T_a}$, respectively as follows:

$$\mathbf{S_a} = \mathbf{A_a'X},$$
$$\mathbf{T_a} = \mathbf{B_a'Y_a},$$

where both $\mathbf{A_a}$ and $\mathbf{B_a}$ are N_{PCA} by N_{CCA} matrices with N_{CCA} CCVs (column vectors) of length N_{PCA}. The n-th CCV transforms the time series of principal components, **X** and $\mathbf{Y_a}$, to n-th canonical score. As a result, $\mathbf{S_a}$ and $\mathbf{T_a}$ are the matrixes with N_{CCA} by N_{trial}. This transformation was done so that the correlations between the canonical scores are maximized (with the built-in function "*canoncorr*" in Matlab).

We have seven time series of the N_{PCA} variables (principal components) in the task-independent spaces, $\mathbf{Y_1}$, $\mathbf{Y_3}$, …, $\mathbf{Y_7}$, from areas Y_1, Y_3, …, Y_7. Then, we can get sets of CCVs, $\mathbf{A_2}$, $\mathbf{A_3}$, …, $\mathbf{A_7}$ and $\mathbf{B_1}$, $\mathbf{B_3}$, …, $\mathbf{B_7}$ and sets of the canonical scores, $\mathbf{S_1}$, $\mathbf{S_3}$, …, $\mathbf{S_7}$ and $\mathbf{T_1}$, $\mathbf{T_3}$, …, $\mathbf{T_7}$.Here, the CCVs of $\mathbf{A_1}$, $\mathbf{A_2}$, …, $\mathbf{A_7}$ defined in the 10-dimensional data space of area **X** correspond to the linear projections of activity of neurons in the area X that best explain the activities of neurons in each of the other areas (7 areas in total). If area X shares similar information with another seven areas, CCVs, $\mathbf{A_1}$, $\mathbf{A_2}$, …, $\mathbf{A_7}$ will be oriented in a similar direction and therefore the length of the sum of the CCVs will be larger. Accordingly, we define the **"information sharing index"** (**Supplementary figure 6e**) of area X as the length of the sum of CCVs as $\max\left(\left|\sum_{i=1}^{7} s_i\, A_{i,d}\right|\right)$, where s_i can be 1 or -1, $A_{i,d}$ is a d-th column vector (CCV) of i-th area, and || denotes the norm.

We also used generalized CCA (GCCA)(Smilde, Måge et al. 2017), which extends the notion of CCA to >2 data sets. We estimated similarity between the first generalized CCV and CCVs for each area by inner product of these vectors. We defined the average of these inner products as **"global information sharing index"** (**Supplementary figure 6f**).

Analysis of Allen connectivity data

We used the Allen Mouse Brain Connectivity Atlas (http://connectivity.brain-map.org; (Oh, Harris et al. 2014)) to investigate the pattern of the corticocortical and thalamocortical projections around the mouse PPC. In this database, connectivity data are available for mice from injection areas (AAV1-EGFP as an anterograde tracer) to any brain region. For estimating the relative projection density between A and AM, the corticocortical projection density was obtained in each layer at 0, 100, 200, 300, 400, 500, 600, 700 μm from pia, averaged and normalized with the injection volume, then averaged across wild-type mice. This was repeated with the major source areas to the A and AM (V1, PM, AL, vRSC, S1t, OFC, dACC, and vACC; **Supplementary figure 8a**). For seed correlation analysis, we downloaded the data whose injection sites were either isocortex (929

experiments) or thalamus (189 experiments) at 100 μm resolution **Supplementary figure 8b**. We set a 100 μm-space grid that covered entire dorsal cortical areas including the PPC. Then, a set of injection sites that projected to each grid at the 300 μm from the surface of the brain were identified for each grid (**Supplementary figure 8c**). Thus, each grid has a set of the injection sites where the grid receives its projection from either isocortex or thalamus. Using these binary connectivity matrixes, we calculated the correlation coefficient between two sets of injection sites of the two grids. Based on this correlation matrixes, we got a map of the correlation coefficient for each grid (seed).

Let a binary data matrix **P** ($N_{pix} \times N_{inj}$) be a set of results of the tracer experiments, where N_{pix} and N_{inj} is the number of pixel (cortical surface) and the number of injection experiments, respectively (**Supplementary figure 8d**). Let **Q** ($N_{pix} \times N_{inj}$) be a set of the injected volume (area), ad let **W** ($N_{pix} \times N_{pix}$) be a pixel-to-pixel connection matrix. By definition,

$$\mathbf{P} = \mathbf{WQ}.$$

Here, we need a correlation matrix, $\mathbf{WW^T}$. However, there are no direct data for **W** or **Q**. Therefore, we estimated it by **P** as follows

$$\mathbf{PP^T} = \mathbf{WQ(WQ)^T} = \mathbf{WQQ^T W^T}.$$

If the injection volume is small and random enough, $\mathbf{QQ^T}$ -> **Id** as the number of experiments gets large. If so, we can approximate $\mathbf{WW^T}$ by $\mathbf{PP^T}$. In reality, $\mathbf{QQ^T}$ should work as a spatial filter of $\mathbf{WW^T}$. As the injection volume would be <500 μm on average, the seed correlation map should capture the structure with a resolution of several hundred micrometers, which would be sufficient for our analysis. This resolution could be improved with decreasing injection volume, or kernel regression (Knox, Harris et al. 2018).

To effectively visualize these maps, we made a software that users can explorer cortical surface point (seed) to see the cortical areas that shared either the corticocortical input, thalamocortical input or both types of input (https://web.ece.ucsb.edu/~riichirohira/TopBM-2.05/index.html).

Statistics

Wilcoxon's rank-sum test and chi-squared test were used for pairwise comparison. For multiple comparison, we used one-way ANOVA and showed confidence intervals (p=0.05) in the figure. No statistical tests were performed to predetermine sample size. No blinding or randomization was performed.

Supplementary Figures

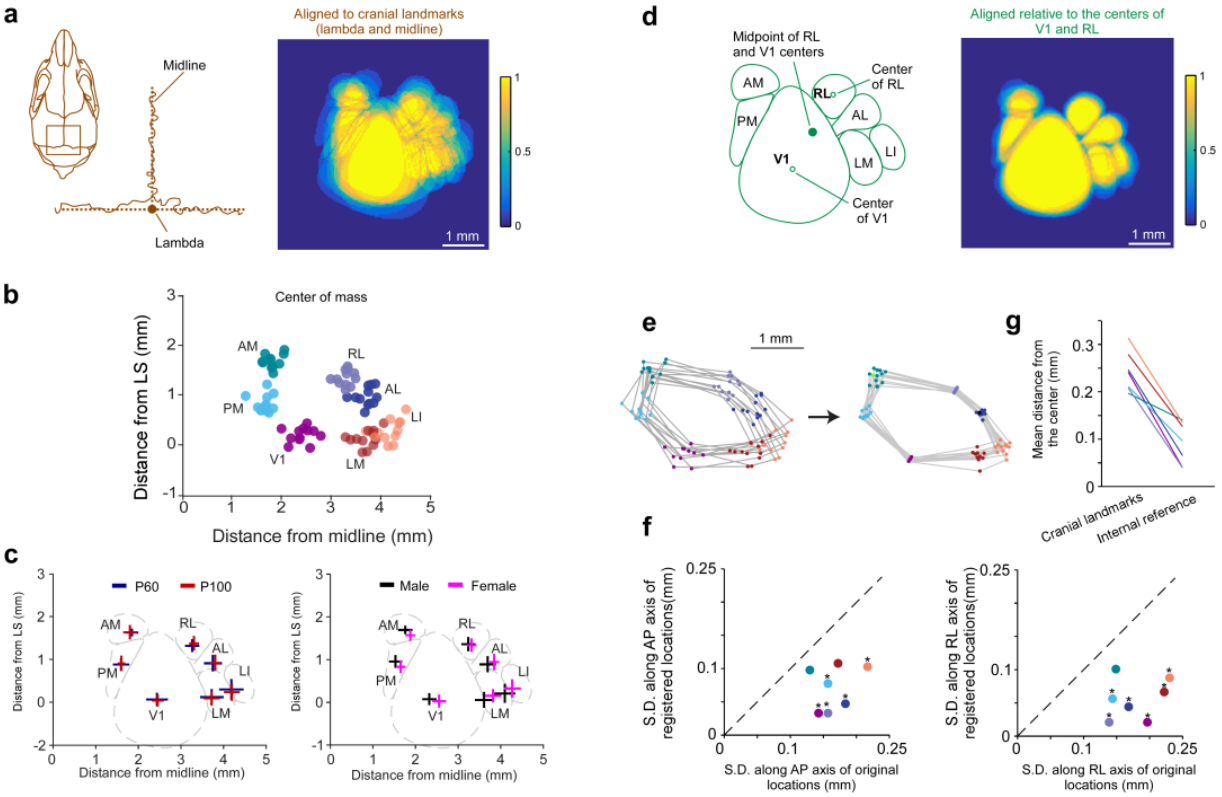

Supplementary Figure 1. **The individual variability of the position of the HVAs. a.** Left, mouse skull and the bony landmarks for reference. We used a midline and a lambda on the skull to register the V1 and HVAs across different mice. Right, overlapped maps of the V1 and HVAs for 12 mice. Note that there is a large variability of HVA locations across mice. **b.** Distribution of the center of mass of V1 and HVAs relative to the midline and lambda. **c.** Comparison of the distribution of the center of mass of V1 and HVAs between different ages (left) and between different sex (right). No significant difference was found (p>0.05, Wilcoxon rank-sum test). The bar indicates ± standard deviation. **d.** Left, we used the midpoint of the center of V1 and the center of RL, and the angle between the midline and the straight line connecting the center of V1 and the center of RL to register the V1 and HVAs across different mice (internal registration). Right, the overlapped maps of the V1 and HVAs for 12 mice. Note that all the HVAs are better registered than the panel **a**, right. **e.** Location of V1 and HVAs before (left) and after (right) the internal registration. The gray lines connect the points from the same mice. The dots colors are the same as panel **b**. **f**. The standard deviation of the location of the center of mass along the anteroposterior and mediolateral axis before and after the internal registration. * p<0.05. ** p<0.01 (Two-sample *F*-test for equal variance). The dots colors are the same as panel **b**. **g**. The mean distance from the center position of each HVA in each mouse to the average center position across mice was compared before and after the registration.

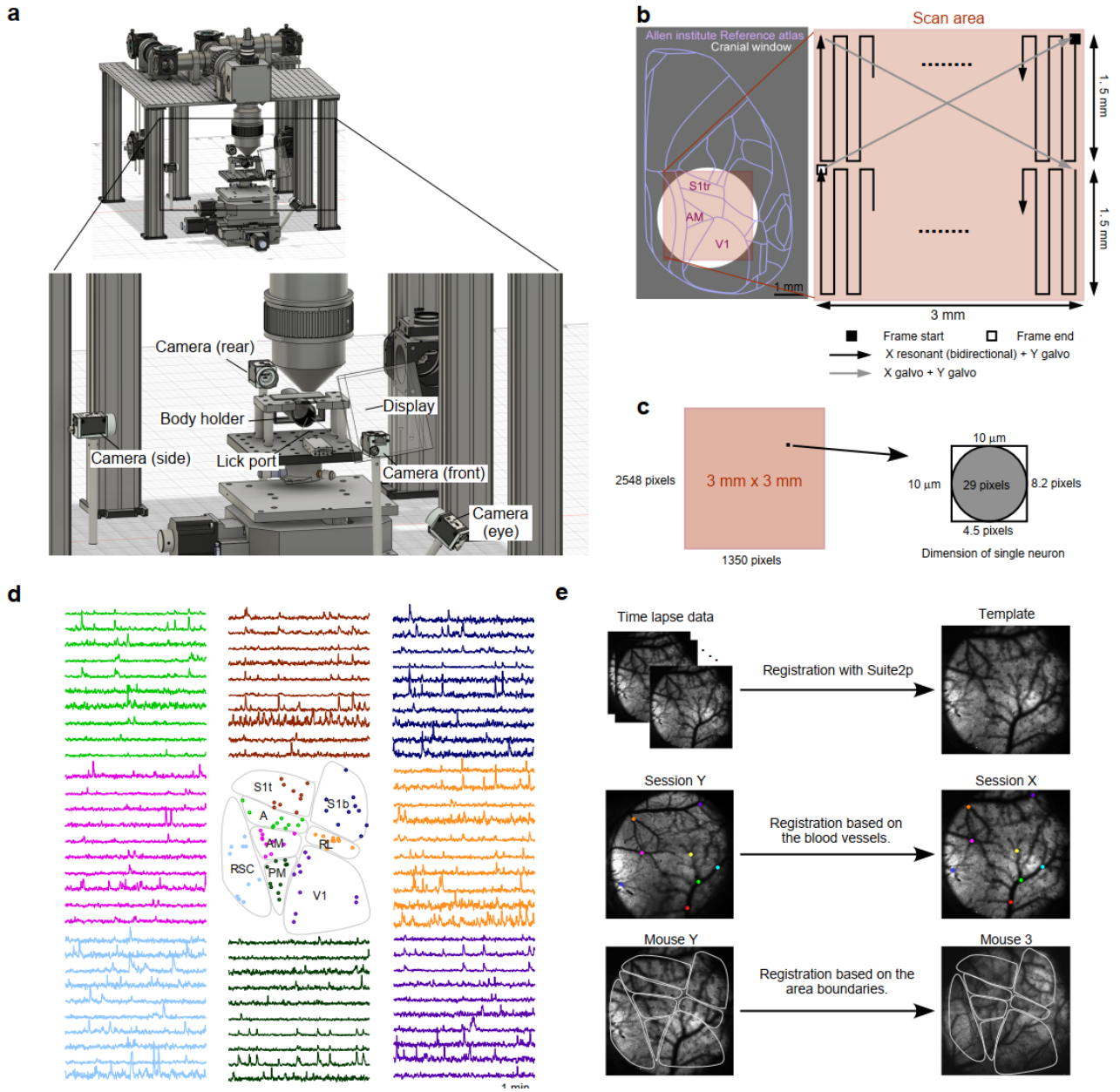

Supplementary Figure 2. A large field-of-view two-photon microscope and its scanning strategy. a. A large field-of-view FOV) two-photon microscope, Diesel2p (Yu, Stirman et al. 2021). Body holder, head-plate holder, display and four cameas are also shown. **b.** Left, the brain areas of the right cerebral cortex of the mouse from Allen atlas (version 3) (Oh, Harris et al. 2014). Right, the scanning strategy to cover the 3 mm by 3 mm square area around the mice PPC. Two 1.5 mm by 3 mm rectangle areas were sequentially scanned using two Galvano scanners and one resonant scanner. **c.** The scanning strategy in panel **b** resulted in 2459 x 1350 pixel^2 for each square frame, which yields 29 pixels (>100 laser pulses) for a circle with a 10 µm diameter (the size single neuron). **d.** Representative activity of simultaneously detected neurons in the same FOV. Ten neurons in 8 areas are shown. Each color of trace corresponds to the area. **e**. Top. The image sequence was registered to the template within a session. Middle. The day-by-day distortion was corrected based on the blood vessels. Bottom. When overlapping the neurons across different mice, we registered images based on the boundaries of areas.

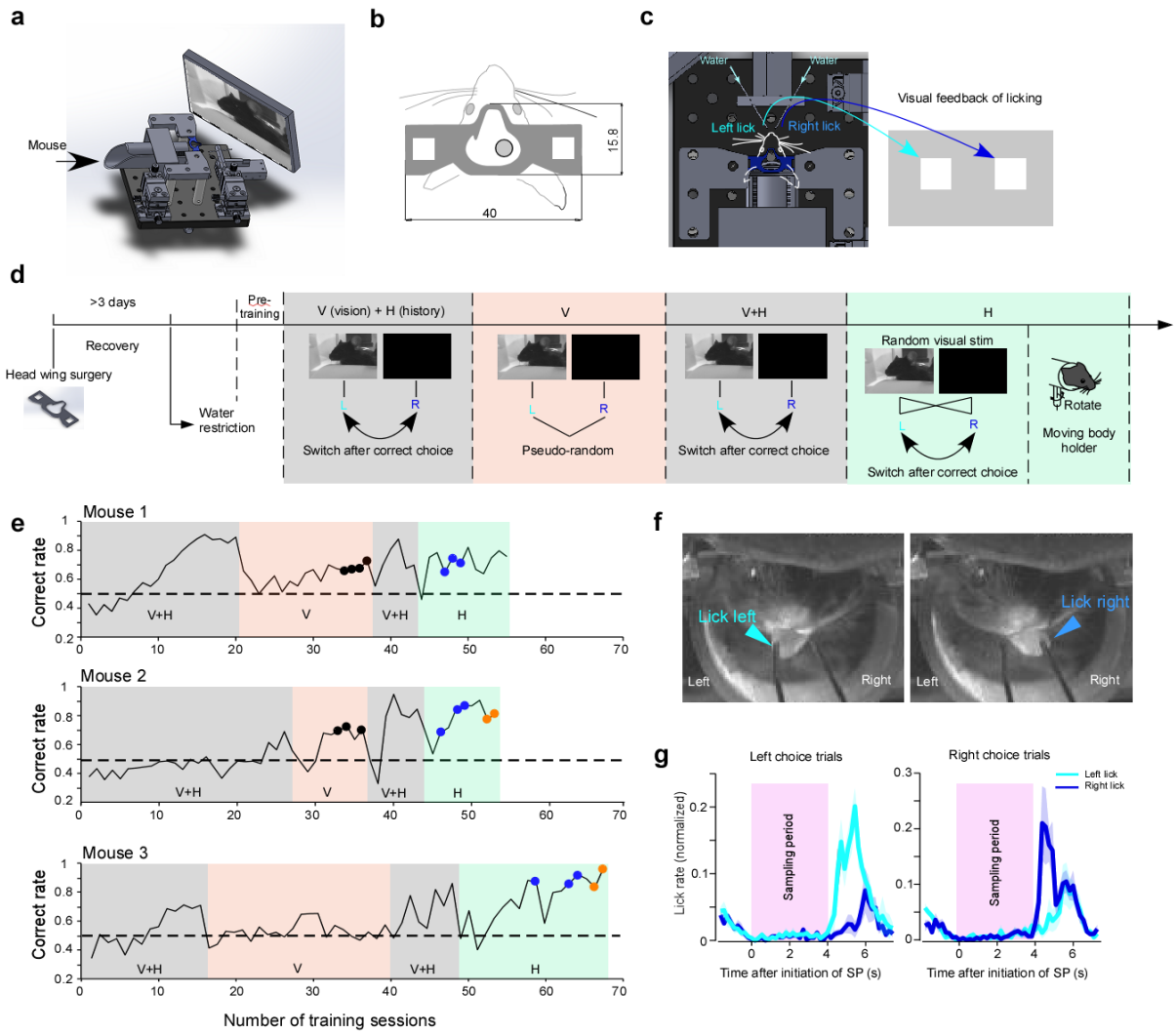

Supplementary Figure 3. Training schedule and learning curves of the tasks for head-fixed mice. **a.** A mouse was head-fixed and held inside a plastic body-holder. The mouse can enter the body-holder smoothly with its head wing into the aperture of the body holder. The display was located at a location covering the left visual field. **b.** The head wing was attached with acrylic resin onto the skull. The dimensions were optimized to observe the PPC of the right hemisphere and to make the mice enter into the body holder smoothly and symmetrically. **c.** A small square at either left or right location in the display was immediately shown (duration: 33 ms) when the mice licked to the left or right licking ports, respectively. **d.** The serial training schedule for multiple tasks. **e.** The correct rates of three example mice were plotted as a function of training sessions. Background color corresponds to the type of the task illustrated in panel **d**. The black, blue and orange dots indicate the imaging experiments of vision task, history task and history task with moving body-holder**. f.** The tongue extension movement during the task was monitored by the video put in front of the mouse (30 fps). Not that this is not necessarily contact between the tongue and spout. We electronically measured contacts of tongue and the spout and used the signal for the choice. **g.** Offline analysis captured the tongue extension to left (left licking, magenta) and tongue to right (right licking, green) during the response period. In both trials with left choice (top panels) and right choice (bottom panels), the tongue extension movements during the sampling period were hardly observed.

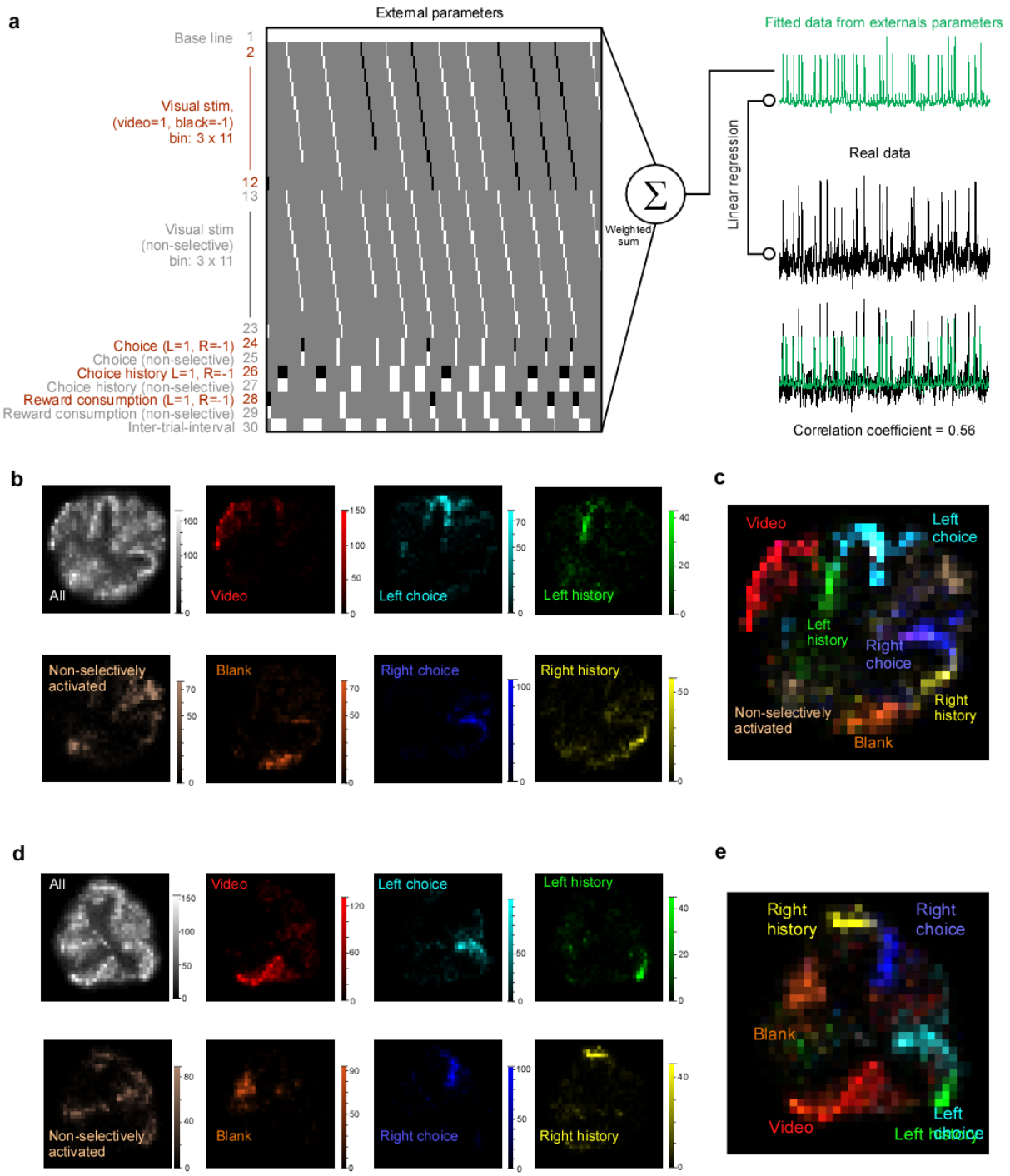

Supplementary Figure 4. Linear encoding models and ratio of neurons that is explained by the behavioral and posture parameters. a. Schematic of a linear encoding model. A weighted sum of 29 external parameters was fitted to the activity of individual neurons. For example, the black trace indicates the activity of a neuron, and the green trace is the output of the linear model. The correlation coefficient of these two was large (0.56), indicating that the model parameters captured the variability of the neuronal activity. The 29 external parameters consisted of times of the visual stimuli (556 ms each, 11 bins, left or right trial), chosen directions (left or right choice), choice histories (3.7 - 7.4 s after left or right choice), reward directions (2 s after rewarded, left or right) and an inter-trial-

interval. A non-selective parameter was also added for each control parameter, to avoid identifying neurons activated both types of the stimuli or the choice as task-related neurons. **b.** The result of *t*-SNE analysis in the vision tasks. The number of neurons within the pixel was color-mapped for each behavior parameter. **c.** Overlayed image of panel **b**. **d.** The result of *t*-SNE analysis in the history tasks. The number of neurons within the pixel was color-mapped for each behavior parameter. **e.** Overlayed image of panel **d**.

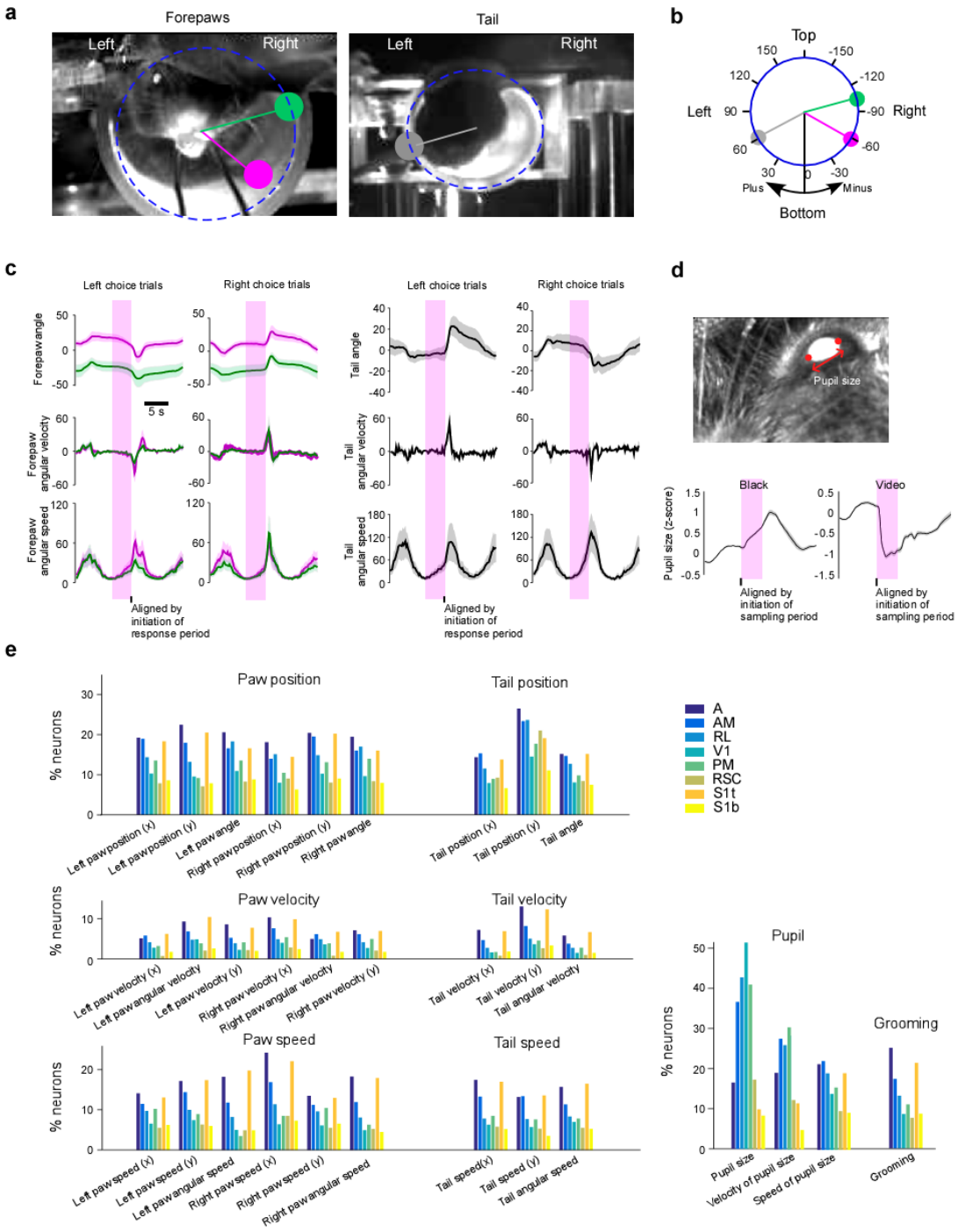

Supplementary Figure 5. Analysis of postures and movements during the task. a. Snapshots from the cameras in front of the mouse (left) and behind the mouse (right). We used the "Deeplabcut", a deep-learning based software for tracking postures of the animals. The green, magenta, and white circles indicate that estimated positions of a right forepaw, a left forepaw, and a tail, respectively, when each part crossed the edge of the body holder. Each line was drawn between each estimated body part and the center of the body holder. Blue circles indicate the edge of the body holder. **b**, Coordinates of the angle of the body parts. **c**. The position, the velocity and

the speed of the three body parts were aligned by the initiation of the response period (RP) for the trials with left and right choice during the mice performing the history task (n=3 mice, total 6 sessions). Shaded areas indicate the sampling period (SP). **d**. Top, the edge of the pupil was identified with the Deeplabcut. Then the size of the pupil was measured as the distance between the two edges. Bottom, the pupil size increased and decreased after the black screen and the natural video started, respectively. **e.** Percentage of neurons in each area that are significantly related to position, speed and velocity of left/right forelimb and tail, size of pupil size, speed and velocity of pupil size, and presence or absence of grooming.

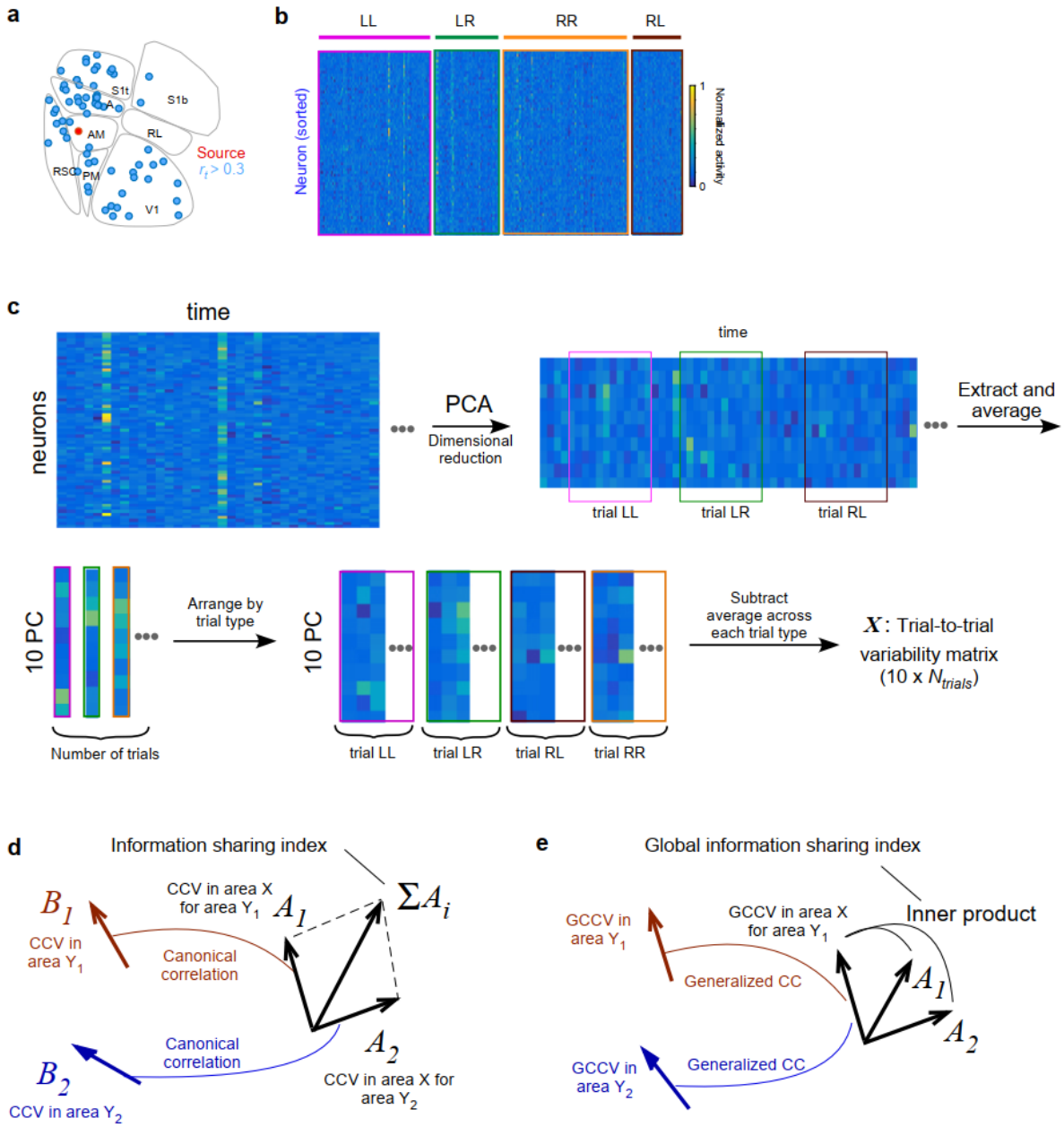

Supplementary Figure 6. Canonical correlation analysis (CCA). **a**. An example source neuron in AM (red) and neurons with $r_t \geq 0.3$ (blue) were shown. **b.** Trial-to-trial activity fluctuation of the highly correlated neurons ($r_t \geq 0.3$, panel b) was color coded in each trial block. **c**.Illustration of CCA pre-processing. Activity of the population of neurons was extracted in each area, and the PCA (principal component analysis) reduced the data dimensions into 10. Then, "fluctuation" activity was calculated similar to the single neuron case. The data during the sampling period of each trial block (**LL**:video/left choice. **LR**:video/right choice. **RR**: black/right choice. **RL**: black/left choice) was extracted and averaged. Then, the residual of the data after subtracting the trial-mean in each trial type was concatenated as a new matrix, ***X*** (one column vector per a PC dimension, that is, 10 x N_{trial} matrix. **d.** Illustration of the canonical correlation analysis and calculation of information sharing index. See methods for the precise definition. **e.** Illustration of the generalized canonical correlation analysis and calculation of global information sharing index. See methods for the precise definition.

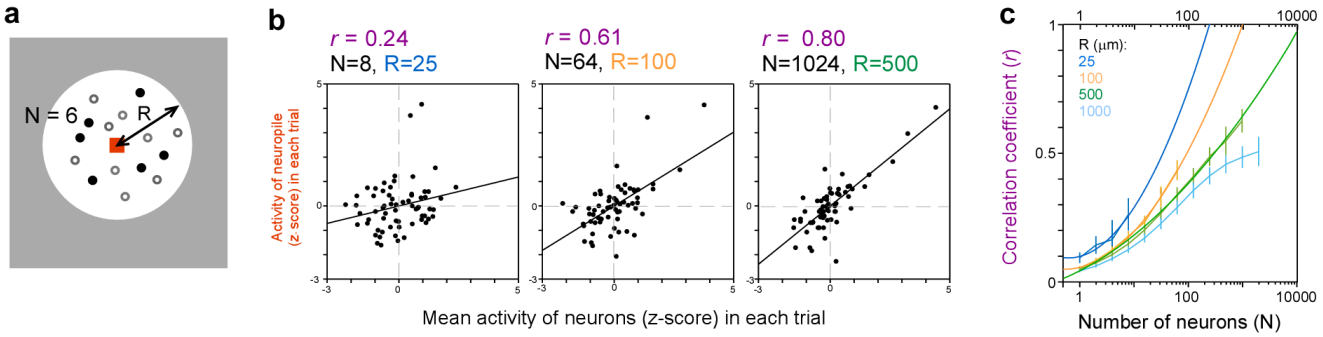

Supplementary Figure 7. The trial-to-trial fluctuation of the neuropil activity and its relation to the single neuron activity. a. To compare the trial-to-trial fluctuation of the neuropil activity and single neuron activity, the single neurons were randomly selected (filled circle) within the distance, R, from the center (red square). Then, the trial-to-trial fluctuation of the neuropil activity at the center and the trial-to-trial fluctuation of the mean activity of selected neurons was compared. **b.** The z-scored neuropil activity in each trial was compared with the z-scored mean activity of *N* selected neurons in the corresponding trial was compared. **c.** The correlation coefficient obtained in the panel **b** was repeatedly calculated with a range of neurons averaged and the distance. The lines show the polynomial fitting curves.

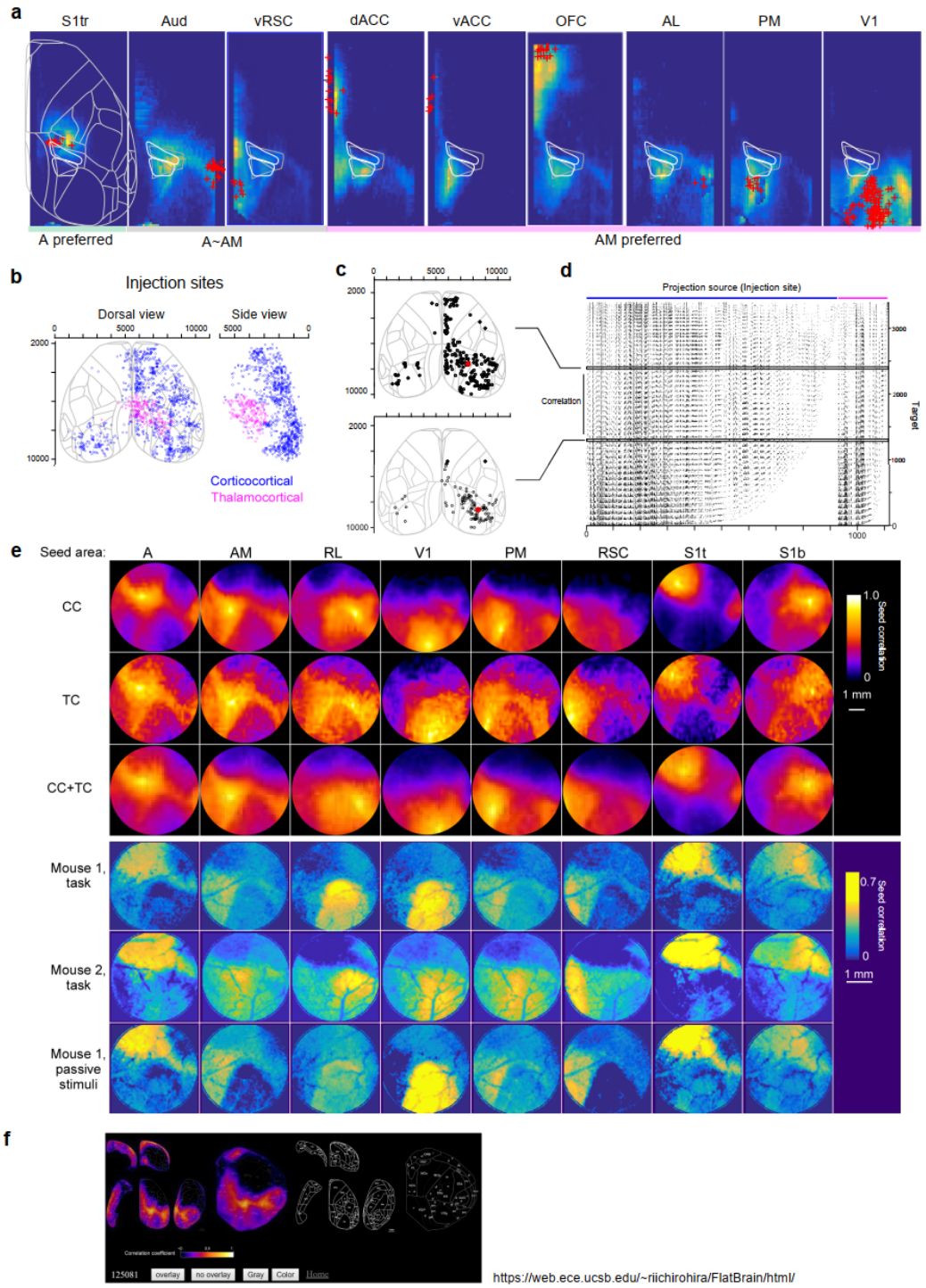

Supplementary Figure 8. Anatomical structure analyzed with anterograde tracer database and its relation to the correlation structure of the trial-to-trial variability in neuropil activity. a. Using Allen connectivity atlas, the axonal density of corticocortical projection was analyzed. The nine cortical areas where A or AM receive the dense are shown. The density was obtained from multiple depths (0, 100, 200, 300, 400, 500, 600, 700 μm from pia), averaged and normalized with the injection volume, then averaged across the experiments. Only the projection from the S1t preferentially distributed in A rather AM. Top-down axons from dACC, vACC, and OFC

preferentially projected to AM rather than A, as well as visual cortices (AL, PM, and V1). Gray boundaries show A and AM in Allen brain atlas, and the white boundaries indicate A and AM in our definition. **b.** Injection sites for cortico-cortical projections (blue) and thalamo-cortical projections (magenta). **c.** Two examples of projection sources (black circles) for a target site (red circle). **d.** A binary matrix **Y** ($N_{pix} \times N_{inj}$). Each column consists of the projection targets of each injection experiment. Two rows indicated by rectangles correspond to the sets of projection sources for the two target sites shown in panel **c. e.** Top and second rows, the correlation between each cortical region and the seed points in each area (A, AM, RL, V1, PM, RSC, S1t, S1b) was color-mapped. The high correlation indicates that the region has highly shared input from the cortex ("CC", top row) or the thalamus ("TC", second row) with the seed region. A dotted circle indicates the imaging area. Second-bottom and bottom, the seed correlation of trial-to-trial activity fluctuation during the vision task ("M2, V", second-bottom row) and during passively viewing the moving bar ("M2, P", bottom row) of mouse 2. Note that all the correlation maps in each column are similar. **f.** A snapshot of the online interactive software, "BrainModules", for exploring the anatomical seed correlation analysis. Link: https://web.ece.ucsb.edu/~riichirohira/TopBM-2.06/index.html

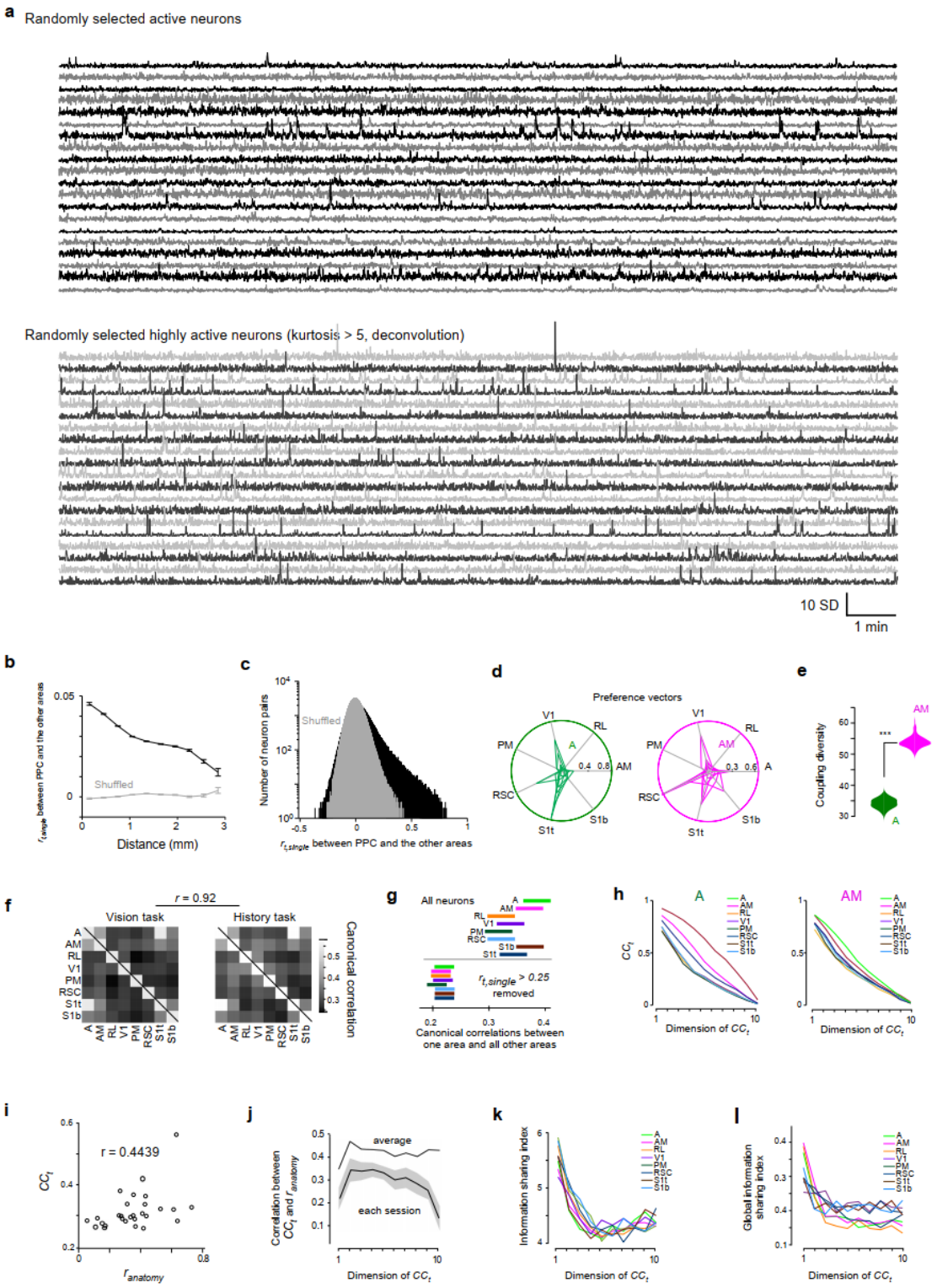

Supplementary Figure 9. a. Randomly selected 20 active neurons (top) and randomly selected 20 highly active neurons (kurtosis > 5, bottom). **b-j.** The same analysis using only highly active neurons (**b: figure 5a.; c: figure 5b; d: figure 5e** ($r_{t,single}$ >0.25)**; e: figure 5f; f: figure 5h; g: figure 6j; j: figure6k; i: figure 6l; j: figure6m**).

References

Akrami, A., C. D. Kopec, M. E. Diamond and C. D. Brody (2018). "Posterior parietal cortex represents sensory history and mediates its effects on behaviour." Nature **554**(7692): 368.
Allen, W. E., I. V. Kauvar, M. Z. Chen, E. B. Richman, S. J. Yang, K. Chan, V. Gradinaru, B. E. Deverman, L. Luo and K. Deisseroth (2017). "Global representations of goal-directed behavior in distinct cell types of mouse neocortex." Neuron **94**(4): 891-907.
Avena-Koenigsberger, A., B. Misic and O. Sporns (2017). "Communication dynamics in complex brain networks." Nat Rev Neurosci **19**(1): 17-33.
Barth, A. M. I. and I. Mody (2011). "Changes in hippocampal neuronal activity during and after unilateral selective hippocampal ischemia in vivo." Journal of Neuroscience **31**(3): 851-860.
Brainard, D. H. (1997). "The Psychophysics Toolbox." Spat Vis **10**(4): 433-436.
Bressler, S. L. and J. A. Kelso (2001). "Cortical coordination dynamics and cognition." Trends Cogn Sci **5**(1): 26-36.
Cavada, C. and P. S. Goldman‐Rakic (1989). "Posterior parietal cortex in rhesus monkey: I. Parcellation of areas based on distinctive limbic and sensory corticocortical connections." Journal of Comparative Neurology **287**(4): 393-421.
Chan, E., N. Kovacevic, S. K. Y. Ho, R. M. Henkelman and J. T. Henderson (2007). "Development of a high resolution three-dimensional surgical atlas of the murine head for strains 129S1/SvImJ and C57Bl/6J using magnetic resonance imaging and micro-computed tomography." Neuroscience **144**(2): 604-615.
Chen, T.-W., T. J. Wardill, Y. Sun, S. R. Pulver, S. L. Renninger, A. Baohan, E. R. Schreiter, R. A. Kerr, M. B. Orger and V. Jayaraman (2013). "Ultrasensitive fluorescent proteins for imaging neuronal activity." Nature **499**(7458): 295-300.
Churchland, M. M., J. P. Cunningham, M. T. Kaufman, J. D. Foster, P. Nuyujukian, S. I. Ryu and K. V. Shenoy (2012). "Neural population dynamics during reaching." Nature **487**(7405): 51-56.
Driscoll, L. N., N. L. Pettit, M. Minderer, S. N. Chettih and C. D. Harvey (2017). "Dynamic reorganization of neuronal activity patterns in parietal cortex." Cell **170**(5): 986-999.
Einevoll, G. T., A. Destexhe, M. Diesmann, S. Grün, V. Jirsa, M. de Kamps, M. Migliore, T. V. Ness, H. E. Plesser and F. Schürmann (2019). "The scientific case for brain simulations." Neuron **102**(4): 735-744.
Engle, J. R. and C. A. Barnes (2012). "Characterizing cognitive aging of associative memory in animal models." Frontiers in aging neuroscience **4**.
Franklin, K. B. J. and G. Paxinos (2001). Paxinos and Franklin's The mouse brain in stereotaxic coordinates.
Freedman, D. J. and G. Ibos (2018). "An integrative framework for sensory, motor, and cognitive functions of the posterior parietal cortex." Neuron **97**(6): 1219-1234.
Froudarakis, E., P. Berens, A. S. Ecker, R. J. Cotton, F. H. Sinz, D. Yatsenko, P. Saggau, M. Bethge and A. S. Tolias (2014). "Population code in mouse V1 facilitates readout of natural scenes through increased sparseness." Nature neuroscience **17**(6): 851.
Funamizu, A., B. Kuhn and K. Doya (2016). "Neural substrate of dynamic Bayesian inference in the cerebral cortex." Nature neuroscience.
Gămănuţ, R., H. Kennedy, Z. Toroczkai, M. Ercsey-Ravasz, D. C. Van Essen, K. Knoblauch and A. Burkhalter (2018). "The mouse cortical connectome, characterized by an ultra-dense cortical graph, maintains specificity by distinct connectivity profiles." Neuron **97**(3): 698-715. e610.
Gilissen, S. R., K. Farrow, V. Bonin and L. Arckens (2021). "Reconsidering the border between the visual and posterior parietal cortex of mice." Cerebral Cortex **31**(3): 1675-1692.
Goard, M. J., G. N. Pho, J. Woodson and M. Sur (2016). "Distinct roles of visual, parietal, and frontal motor cortices in memory-guided sensorimotor decisions." Elife **5**: e13764.

Han, Y., J. M. Kebschull, R. A. Campbell, D. Cowan, F. Imhof, A. M. Zador and T. D. Mrsic-Flogel (2018). "The logic of single-cell projections from visual cortex." Nature **556**(7699): 51-56.
Harvey, C. D., P. Coen and D. W. Tank (2012). "Choice-specific sequences in parietal cortex during a virtual-navigation decision task." Nature **484**(7392): 62-68.
Hattori, R., B. Danskin, Z. Babic, N. Mlynaryk and T. Komiyama (2019). "Area-Specificity and Plasticity of History-Dependent Value Coding During Learning." Cell.
Hira, R., F. Ohkubo, K. Ozawa, Y. Isomura, K. Kitamura, M. Kano, H. Kasai and M. Matsuzaki (2013). "Spatiotemporal dynamics of functional clusters of neurons in the mouse motor cortex during a voluntary movement." Journal of Neuroscience **33**(4): 1377-1390.
Hovde, K., M. Gianatti, M. P. Witter and J. R. Whitlock (2018). "Architecture and organization of mouse posterior parietal cortex relative to extrastriate areas." Eur J Neurosci.
Itokazu, T., M. Hasegawa, R. Kimura, H. Osaki, U.-R. Albrecht, K. Sohya, S. Chakrabarti, H. Itoh, T. Ito and T. K. Sato (2018). "Streamlined sensory motor communication through cortical reciprocal connectivity in a visually guided eye movement task." Nature communications **9**(1): 338.
Kalatsky, V. A. and M. P. Stryker (2003). "New paradigm for optical imaging: temporally encoded maps of intrinsic signal." Neuron **38**(4): 529-545.
Kerr, J. N. D., D. Greenberg and F. Helmchen (2005). "Imaging input and output of neocortical networks in vivo." Proceedings of the National Academy of Sciences **102**(39): 14063-14068.
Kleiner, M., D. H. Brainard and D. G. Pelli (2007). ""What's new in Psychtoolbox-3?"." Perception **36**.
Knox, J. E., K. D. Harris, N. Graddis, J. D. Whitesell, H. Zeng, J. A. Harris, E. Shea-Brown and S. Mihalas (2018). "High-resolution data-driven model of the mouse connectome." Network Neuroscience **3**(1): 217-236.
Krumin, M., J. J. Lee, K. D. Harris and M. Carandini (2018). "Decision and navigation in mouse parietal cortex." ELife **7**: e42583.
Kwon, S. E., H. Yang, G. Minamisawa and D. H. O'Connor (2016). "Sensory and decision-related activity propagate in a cortical feedback loop during touch perception." Nature neuroscience **19**(9): 1243.
Lyamzin, D. and A. Benucci (2019). "The mouse posterior parietal cortex: anatomy and functions." Neuroscience research **140**: 14-22.
Madisen, L., A. R. Garner, D. Shimaoka, A. S. Chuong, N. C. Klapoetke, L. Li, A. Van Der Bourg, Y. Niino, L. Egolf and C. Monetti (2015). "Transgenic mice for intersectional targeting of neural sensors and effectors with high specificity and performance." Neuron **85**(5): 942-958.
Manita, S., T. Suzuki, C. Homma, T. Matsumoto, M. Odagawa, K. Yamada, K. Ota, C. Matsubara, A. Inutsuka and M. Sato (2015). "A top-down cortical circuit for accurate sensory perception." Neuron **86**(5): 1304-1316.
Marshel, J. H., M. E. Garrett, I. Nauhaus and E. M. Callaway (2011). "Functional specialization of seven mouse visual cortical areas." Neuron **72**(6): 1040-1054.
Mathis, A., P. Mamidanna, K. M. Cury, T. Abe, V. N. Murthy, M. W. Mathis and M. Bethge (2018). DeepLabCut: markerless pose estimation of user-defined body parts with deep learning, Nature Publishing Group.
McGinley, M. J., M. Vinck, J. Reimer, R. Batista-Brito, E. Zagha, C. R. Cadwell, A. S. Tolias, J. A. Cardin and D. A. McCormick (2015). "Waking State: Rapid Variations Modulate Neural and Behavioral Responses." Neuron **87**(6): 1143-1161.
Mimica, B., B. A. Dunn, T. Tombaz, V. S. Bojja and J. R. Whitlock (2018). "Efficient cortical coding of 3D posture in freely behaving rats." Science **362**(6414): 584-589.
Minderer, M., K. D. Brown and C. D. Harvey (2019). "The Spatial Structure of Neural Encoding in Mouse Posterior Cortex during Navigation." Neuron.
Mohan, H., R. de Haan, R. Broersen, A. W. Pieneman, F. Helmchen, J. F. Staiger, H. D. Mansvelder and C. P. J. de Kock (2019). "Functional architecture and encoding of tactile sensorimotor behavior in rat posterior parietal cortex." Journal of Neuroscience: 0693-0619.

Morcos, A. S. and C. D. Harvey (2016). "History-dependent variability in population dynamics during evidence accumulation in cortex." Nature neuroscience **19**(12): 1672.
Neske, G. T. (2015). "The Slow Oscillation in Cortical and Thalamic Networks: Mechanisms and Functions." Front Neural Circuits **9**: 88.
Odoemene, O., H. Nguyen and A. K. Churchland (2017). "Visual evidence accumulation behavior in unrestrained mice." bioRxiv: 195792.
Odoemene, O., S. Pisupati, H. Nguyen and A. K. Churchland (2018). "Visual evidence accumulation guides decision-making in unrestrained mice." Journal of Neuroscience **38**(47): 10143-10155.
Oh, S. W., J. A. Harris, L. Ng, B. Winslow, N. Cain, S. Mihalas, Q. Wang, C. Lau, L. Kuan and A. M. Henry (2014). "A mesoscale connectome of the mouse brain." Nature **508**(7495): 207.
Olcese, U., G. Iurilli and P. Medini (2013). "Cellular and synaptic architecture of multisensory integration in the mouse neocortex." Neuron **79**(3): 579-593.
Olsen, G. M. and M. P. Witter (2016). "Posterior parietal cortex of the rat: Architectural delineation and thalamic differentiation." Journal of Comparative Neurology **524**(18): 3774-3809.
Pachitariu, M., C. Stringer, M. Dipoppa, S. Schröder, L. F. Rossi, H. Dalgleish, M. Carandini and K. D. Harris (2017). "Suite2p: beyond 10,000 neurons with standard two-photon microscopy." Biorxiv: 061507.
Pho, G. N., M. J. Goard, J. Woodson, B. Crawford and M. Sur (2018). "Task-dependent representations of stimulus and choice in mouse parietal cortex." Nature communications **9**(1): 2596.
Raposo, D., M. T. Kaufman and A. K. Churchland (2014). "A category-free neural population supports evolving demands during decision-making." Nature neuroscience **17**(12): 1784.
Rasmussen, R. N., A. Asiminas, E. M. M. Carlsen, C. Kjaerby and N. A. Smith (2023). "Astrocytes: integrators of arousal state and sensory context." Trends Neurosci **46**(6): 418-425.
Reep, R. L. and J. V. Corwin (2009). "Posterior parietal cortex as part of a neural network for directed attention in rats." Neurobiology of learning and memory **91**(2): 104-113.
Rizzolatti, G., L. Fogassi and V. Gallese (1997). "Parietal cortex: from sight to action." Current opinion in neurobiology **7**(4): 562-567.
Runyan, C. A., E. Piasini, S. Panzeri and C. D. Harvey (2017). "Distinct timescales of population coding across cortex." Nature **548**(7665): 92.
Schindelin, J., I. Arganda-Carreras, E. Frise, V. Kaynig, M. Longair, T. Pietzsch, S. Preibisch, C. Rueden, S. Saalfeld, B. Schmid, J. Y. Tinevez, D. J. White, V. Hartenstein, K. Eliceiri, P. Tomancak and A. Cardona (2012). "Fiji: an open-source platform for biological-image analysis." Nat Methods **9**(7): 676-682.
Schindelin, J., C. T. Rueden, M. C. Hiner and K. W. Eliceiri (2015). "The ImageJ ecosystem: An open platform for biomedical image analysis." Mol Reprod Dev **82**(7-8): 518-529.
Schneider, C. A., W. S. Rasband and K. W. Eliceiri (2012). "NIH Image to ImageJ: 25 years of image analysis." Nat Methods **9**(7): 671-675.
Slotnick, B. (2009). "A simple 2-transistor touch or lick detector circuit." Journal of the experimental analysis of behavior **91**(2): 253.
Smilde, A. K., I. Måge, T. Naes, T. Hankemeier, M. A. Lips, H. A. Kiers, E. Acar and R. Bro (2017). "Common and distinct components in data fusion." Journal of Chemometrics **31**(7): e2900.
Smith, I. T., L. B. Townsend, R. Huh, H. Zhu and S. L. Smith (2017). "Stream-dependent development of higher visual cortical areas." Nature neuroscience **20**(2): 200-208.
Smith, S. L. and J. T. Trachtenberg (2007). "Experience-dependent binocular competition in the visual cortex begins at eye opening." Nature neuroscience **10**(3): 370.
Song, Y.-H., J.-H. Kim, H.-W. Jeong, I. Choi, D. Jeong, K. Kim and S.-H. Lee (2017). "A neural circuit for auditory dominance over visual perception." Neuron **93**(4): 940-954.
Spring, S., J. P. Lerch and R. M. Henkelman (2007). "Sexual dimorphism revealed in the structure of the mouse brain using three-dimensional magnetic resonance imaging." Neuroimage **35**(4): 1424-1433.
Stirman, J. N., I. T. Smith, M. W. Kudenov and S. L. Smith (2016). "Wide field-of-view, multi-region, two-photon imaging of neuronal activity in the mammalian brain." Nature Biotechnology **34**(8): 857-862.

Stringer, C., M. Pachitariu, N. Steinmetz, C. B. Reddy, M. Carandini and K. D. Harris (2019). "Spontaneous behaviors drive multidimensional, brainwide activity." Science **364**(6437): 255.
Sussillo, D., M. M. Churchland, M. T. Kaufman and K. V. Shenoy (2015). "A neural network that finds a naturalistic solution for the production of muscle activity." Nature neuroscience **18**(7): 1025.
Tseng, S.-Y., S. N. Chettih, C. Arlt, R. Barroso-Luque and C. D. Harvey (2022). "Shared and specialized coding across posterior cortical areas for dynamic navigation decisions." Neuron **110**(15): 2484-2502. e2416.
Vogelstein, J. T., A. M. Packer, T. A. Machado, T. Sippy, B. Babadi, R. Yuste and L. Paninski (2010). "Fast nonnegative deconvolution for spike train inference from population calcium imaging." Journal of neurophysiology **104**(6): 3691-3704.
Wang, Q. and A. Burkhalter (2007). "Area map of mouse visual cortex." J Comp Neurol **502**(3): 339-357.
Wang, Q., S.-L. Ding, Y. Li, J. Royall, D. Feng, P. Lesnar, N. Graddis, M. Naeemi, B. Facer and A. Ho (2020). "The Allen mouse brain common coordinate framework: a 3D reference atlas." Cell **181**(4): 936-953. e920.
Waters, J., E. Lee, N. Gaudreault, F. Griffin, J. Lecoq, C. Slaughterbeck, D. Sullivan, C. Farrell, J. Perkins and D. Reid (2019). "Biological variation in the sizes, shapes and locations of visual cortical areas in the mouse." PloS one **14**(5): e0213924.
Whitlock, J. R., R. J. Sutherland, M. P. Witter, M.-B. Moser and E. I. Moser (2008). "Navigating from hippocampus to parietal cortex." Proceedings of the National Academy of Sciences **105**(39): 14755-14762.
Yang, F. C., T. K. Jacobson and R. D. Burwell (2017). "Single neuron activity and theta modulation in the posterior parietal cortex in a visuospatial attention task." Hippocampus **27**(3): 263-273.
Yoshitake, K., H. Tsukano, M. Tohmi, S. Komagata, R. Hishida, T. Yagi and K. Shibuki (2013). "Visual map shifts based on whisker-guided cues in the young mouse visual cortex." Cell reports **5**(5): 1365-1374.
Yu, C.-H., J. N. Stirman, Y. Yu, R. Hira and S. L. Smith (2021). "Diesel2p mesoscope with dual independent scan engines for flexible capture of dynamics in distributed neural circuitry." Nature communications **12**(1): 6639.
Yu, Y., J. N. Stirman, C. R. Dorsett and S. L. Smith (2018). "Mesoscale correlation structure with single cell resolution during visual coding." bioRxiv: 469114.
Zhong, L., Y. Zhang, C. A. Duan, J. Pan and N.-l. Xu (2018). "Dynamic and causal contribution of parietal circuits to perceptual decisions during category learning." bioRxiv: 304071.